



AN X-RAY SPECTRAL MODEL OF REPROCESSING BY SMOOTH AND CLUMPY MOLECULAR TORI IN ACTIVE GALACTIC NUCLEI WITH THE MONACO FRAMEWORK

SHUN'YA FURUI¹, YASUSHI FUKAZAWA^{1,2,3}, HIROKAZU ODAKA^{4,5}, TOSHIHIRO KAWAGUCHI⁶, MASANORI OHNO^{1,3}, AND KAZUMA HAYASHI¹

¹ Department of Physical Science, Hiroshima University, 1-3-1 Kagamiyama, Higashi-Hiroshima, Hiroshima 739-8526, Japan

² Hiroshima Astrophysical Science Center, Hiroshima University, 1-3-1 Kagamiyama, Higashi-Hiroshima,

Hiroshima 739-8526, Japan; fukazawa@hep01.hepl.hiroshima-u.ac.jp

³ Core Research for Energetic universe (Core-U), Hiroshima University, 1-3-1 Kagamiyama, Higashi-Hiroshima, Hiroshima 739-8526, Japan

⁴ Kavli Institute for Particle Astrophysics and Cosmology, Stanford University, 2575 Sand Hill Rd, Menlo Park, CA 94025, USA

⁵ Institute of Space and Astronautical Science (ISAS), Japan Aerospace Exploration Agency (JAXA), 3-1-1 Yoshinodai, Chuo, Sagami-hara, Kanagawa, 252-5210, Japan

⁶ Department of Liberal Arts and Sciences, Sapporo Medical University, S1W17, Chuo-ku, Sapporo 060-8556, Japan

Received 2015 November 2; accepted 2016 January 4; published 2016 February 17

ABSTRACT

We construct an X-ray spectral model of reprocessing by a torus in an active galactic nucleus (AGN) with the Monte Carlo simulation framework MONACO. Two torus geometries of smooth and clumpy cases are considered and compared. In order to reproduce a Compton shoulder accurately, MONACO includes not only free electron scattering but also bound electron scattering. Raman and Rayleigh scattering are also treated, and scattering cross sections dependent on chemical states of hydrogen and helium are included. Doppler broadening by turbulence velocity can be implemented. Our model gives results consistent with other available models, such as MYTORUS, except for differences due to different physical parameters and assumptions. We studied the dependence on torus parameters for a Compton shoulder, and found that a intensity ratio of a Compton shoulder to the line core mainly depends on column density, inclination angle, and metal abundance. For instance, an increase of metal abundance makes a Compton shoulder relatively weak. Also, the shape of a Compton shoulder depends on the column density. Furthermore, these dependences become different between smooth and clumpy cases. Then, we discuss the possibility of ASTRO-H/SXS spectroscopy of Compton shoulders in AGN reflection spectra.

Key words: galaxies: active – X-rays: galaxies

1. INTRODUCTION

Active galactic nuclei (AGNs) have supermassive black holes (SMBHs) at the center of each galaxy, and accretion discs surrounding the SMBHs emit an enormous energy of 10^{42} – 10^{47} erg s^{-1} from a region whose size is as small as the solar system. Based on various observational results, a huge gas-dust structure, so-called “torus,” presumably exists around the accretion disc (Antonucci & Miller 1985), and hides the central engine with a substantial fraction from distant observers. The torus is likely composed of inflowing materials from a parent galaxy to an accretion disc and is thus related to the evolution of an SMBH. For the X-ray radiation of an AGN, we observe not only a direct (e.g., transmitted) component from the accretion disc/corona but also a reprocessed component by the torus. The reprocessed component contains information such as X-ray fluorescence, absorption, and reflection (e.g., Awaki et al. 1991; Fukazawa et al. 2011). Therefore, it is important to clarify what can be learned about the state of matter (e.g., temperature, degree of ionization, and velocity dispersion) via the observed X-ray spectra.

In order to estimate the state of materials in the tori, various X-ray spectral models have been constructed and compared with the observed data. Among them, a commonly used model is *pexrav* (Magdziarz & Zdziarski 1995) in XSPEC. This is the reflection model from a flat infinite disc, but fluorescence lines are not included in this model. The model is improved (*pexmon*; Nandra et al. 2007) by adding fluorescence lines to the *pexrav* model. Furthermore, more complicated models are available (Ikeda et al. 2009; Murphy & Yaqoob 2009; Brightman & Nandra 2011), and Liu & Li (2014, 2015) have

begun to study X-ray spectra from AGN tori with *Geant4*, a widely used Monte Carlo simulation library in fields ranging from high-energy particle physics to space science (Ivanchenko et al. 2003). As seen in these models, more realistic shapes of the torus and physical processes have been developed in recent years, and they enable us to estimate the state of materials in detail. Brightman et al. (2015) reported some comparisons of the models of reprocessing by tori among *pexrav*, *MYTORUS* (Murphy & Yaqoob 2009), and the model of Brightman & Nandra (2011). However, most of these models fall under any of the following: the distribution of material is smooth, only simple geometry is discussed, and the effects of velocity dispersion and/or scattering with bound electrons are not considered.

To sustain the geometrical thickness of the torus, the velocity dispersion must be as large as a typical rotation velocity of the torus, ~ 100 km s^{-1} . However, the thermal velocity of this dusty gas cannot become fast up to this speed, because dust grains reach the sublimation temperature $T \sim 1500$ K (Barvainis 1987; Laor & Draine 1993). Therefore, the torus is most likely a group of many dusty clumps with a large velocity dispersion (clumpy torus), rather than a smooth mixture of gas and dust (smooth torus; Krolik & Begelman 1988). Although simple geometries (e.g., smooth gas fulfilled in doughnuts) have been applied in most torus models for X-ray studies, an actual torus is likely (1) clumpy, and (2) has a concave shape at the innermost region because of anisotropic emissions from the accretion disc (Kawaguchi & Mori 2010, 2011). Moreover, (3) the velocity dispersion of the innermost part is as high as thousands of km s^{-1} (Kawaguchi 2013), which inevitably

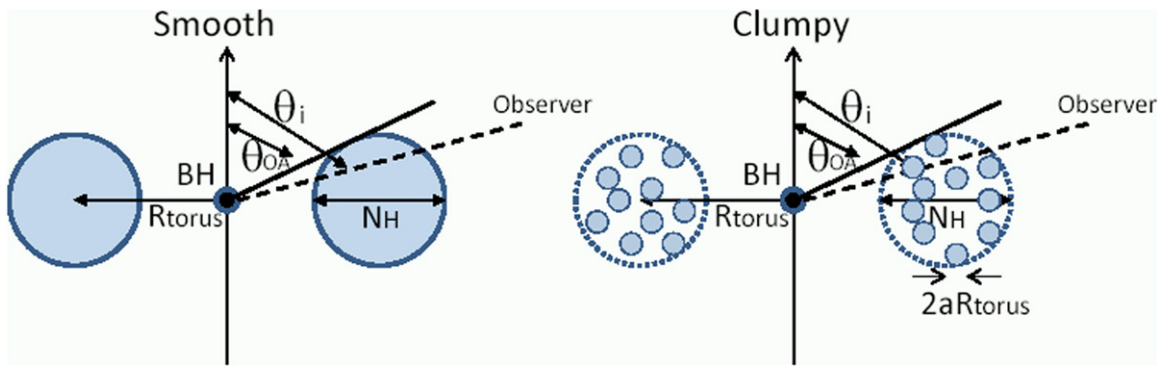


Figure 1. Torus geometry implemented in our model for smooth (left) and clumpy (right) cases. Inclination angle θ_i , opening angle θ_{OA} , torus radius R_{torus} , and column density N_H are also shown.

affects the interpretations and predictions for future high-resolution spectroscopy, which will be realized by the *ASTRO-H* X-ray observatory, scheduled for launch in 2016 (Takahashi et al. 2014).

All these realistic geometrical configurations and kinematics should be considered for the analysis of high-resolution spectra. In order to build such a realistic spectral model, we must solve a problem of radiative transfer that requires treatment of a discrete process of a photon, competing processes, and multiple interactions in a complicated geometry. This is obviously difficult using analytical methods, and we therefore adopt the *MYTorus* project as a Monte Carlo approach (Murphy & Yaqoob 2009). As the first step of this project, this paper focuses on the effects of the clumpiness and the velocity dispersion, though we still use a simple geometry of the entire torus, which is adopted in *MYTorus*. Our simulation model is constructed with a Monte Carlo simulation framework, *MONACO* (MONte Carlo simulation for Astrophysics and COsmology), which was originally developed and verified in the context of X-ray reflection nebulae in the Galactic Center region (Odaka et al. 2011).

In the Compton-thick reflection case, a conspicuous feature, the so-called Compton shoulder, is formed adjacent to emission lines, after the scattering of line photons. Since the shape of a Compton shoulder changes with various parameters such as the state of a scattering electron (free or bound, etc.) and the kinematics of materials, the Compton shoulder is a strong probe to investigate the state of matter around the black hole (Murphy & Yaqoob 2009). Matt (2002) presented the dependence of the Compton shoulder against the column density and inclination angle, but only for the reflector geometry of a sphere or plane. Yaqoob & Murphy (2011) studied the Compton shoulder for the reflector geometry of a smooth torus, and mainly showed the dependence of the Compton shoulder shape on the column density, inclination, incident spectral slope, and velocity dispersion. Our simulator based on *MOCACO* includes accurate physical processes considering Compton scattering not only by free electrons but also bound electrons in atoms or molecules for hydrogen and helium. Since these processes are not included properly in other works, we are able to investigate the shape of a Compton shoulder more accurately and in detail. In addition, we for the first time study the Compton shoulder for the clumpy torus.

In this work, we present the results of simulations on a smooth and a clumpy torus and discuss the effects of

clumpiness. We explain the torus geometry, the Monte Carlo code, and the simulation process in Section 2. We present the results of the reflection continuum and Compton shoulder in Section 3, followed by discussions in Section 4.

2. MODELS AND CALCULATION METHODS

2.1. Torus Geometry and Material Properties

We construct both smooth and clumpy torus models for the Monte Carlo simulations. Figure 1 shows the cross-section view of these tori: the smooth one is shown in the left panel and the clumpy one in the right. In the both models, matter is distributed in a common torus geometry that is determined by the opening angle θ_{OA} and the major radius R_{torus} of the torus surrounding the central black hole. The smooth torus has a uniform hydrogen number density n_H and therefore the column density measured along a line on the equatorial plane from the central black hole is given by $N_H = 2n_H R_{torus} \cos \theta_{OA}$. We assume the chemical composition of solar values obtained by Anders & Grevesse (1989), and elemental abundances of metals (lithium and heavier elements) can be scaled by a common factor A_{metal} (metal abundance relative to the solar values). In addition, the simulation is able to treat Doppler effects due to the random motion of the torus material. The gas motion is treated as micro-turbulence for simplicity, so the gas velocity has a Gaussian distribution with a standard deviation of v_{turb} , which is called a turbulent velocity.

The clumpy torus consists of a number of small spherical clumps all of which have common radius, density, and chemical composition. These clumps are randomly distributed in the torus geometry identical to the one adopted in the smooth torus model. The positions of the clumps are randomly determined so as to keep uniformity of the torus. Then, if there are geometrical overlaps between the clumps, the conflicting clumps are rearranged in order to define clumps as geometrically separate objects. We introduce a clump scaling factor a , which determines the clump radius as $R_{clump} = aR_{torus}$. The degree of clumpiness is characterized by a volume filling factor f , which is defined as a fraction of volume that is filled with the clumps in the whole torus volume. The number of clumps is calculated to be $fV_{torus}/V_{clump} = (3/2)f\pi a^{-3} \cos^2 \theta_{OA}$, where we use the torus volume $V_{torus} = 2\pi^2 R_{torus}^3 \cos^2 \theta_{OA}$ and the clump volume $V_{clump} = (4/3)\pi R_{clump}^3$. The hydrogen number density n_H in a single clump should be enhanced by a factor of f^{-1} from the

Table 1
Independent Model Parameters

Common Parameters	Range
Torus opening angle θ_{OA}	60°
Column density N_{H}	$1 \times 10^{21} - 1 \times 10^{26} \text{ cm}^{-2}$
Metal abundance A_{metal}	0.1–10 solar
Turbulent velocity v_{turb}	0–3000 km s^{-1}
Additional Parameters of Clumpy Torus	Range
Clump scaling factor a	0.002–0.005
Volume filling factor f	0.01–0.05

number density averaged over the whole torus, namely, we have a relation $N_{\text{H}} = 2fn_{\text{H}}R_{\text{torus}} \cos \theta_{\text{OA}}$.

The average number of clumps along a radial equatorial direction is calculated by the product of the clump density in a unit volume [$f/(4\pi R_{\text{clump}}^3/3)$], the cross section of one clump (πR_{clump}^2) and the length of the region where clumps are located ($2R_{\text{torus}} \cos \theta_{\text{OA}}$) (e.g., Kawaguchi & Mori 2011, Equation (A6)). With our fiducial parameters, it is $7.5(f/0.05)(a/0.005)^{-1}(\cos \theta_{\text{OA}}/0.5)$, within the probable range of this quantity (5–15) estimated by Nenkova et al. (2008).

Hydrogen can exist in a state of atoms or molecules. Although both forms can be treated in the same way for most photon interactions, only Rayleigh scattering for molecular hydrogen should be enhanced by a factor of two per electron because of coherent effects (Sunyaev & Churazov 1996). Our simulation code is able to treat both atomic hydrogen and molecular hydrogen. Most hydrogens within each clump likely form molecules (e.g., Pier & Voit 1995). For instance, the temperature inside a clump even at the innermost edge of the torus is around 500 K or less (Hönig et al. 2006, their Figure 4 and Table 1). Although hard X-ray photons can reach deep into each clump, a large fraction (33%–95%) of hydrogen within a clump forms molecules (Krolik & Lepp 1989, their Table 2). In this paper, we assume that all hydrogen exists as H_2 molecules.

In short, our model is specified by the geometry of the torus and the material properties (i.e., the chemical composition and the turbulent velocity). Essentially, the column density controls the total amount of the matter; thus, we do not need to care about the absolute size of the system. In Table 1, we summarize the independent model parameters of the smooth torus model as well as additional parameters of the clumpy torus model.

2.2. Monte Carlo Code and Photon Interactions

A Monte Carlo approach is suitable for solving radiative transfer in the AGN torus since multiple interactions must be treated in a complicated optically thick geometry. For our simulations, we use MONACO (Odaka et al. 2011), a Monte Carlo calculation framework of X-ray radiation for general astrophysical problems. This code utilizes the Geant4 toolkit library (Agostinelli et al. 2003; Allison et al. 2006) for tracking photons in a complicated geometry. Although Geant4 already has its own physical process libraries mainly for radiation measurements, we do not use them but introduce our original physics implementations required for astrophysical purposes. Several photon processes that play important roles in

astrophysics—e.g., photoelectric absorption, scattering, photoionization, photoexcitation, and Comptonization—are included in MONACO and we select the necessary processes among them for the purpose of the simulation. MONACO is able to treat a variety of geometries composed of neutral matter as well as ionized plasma. The Doppler shift and broadening due to bulk and random (thermal and turbulent) motions are also calculated in the photon tracking calculation.

Physics implementation used in this work was originally developed and was verified in the context of X-ray reflection from molecular clouds by Odaka et al. (2011). As described in Section 2.1, we assume that matter in the torus is cold and hydrogens are all in molecular forms. In this condition, we need to consider photoelectric absorption followed by a fluorescence emission and scattering by an electron that is bound to hydrogen and helium as the interactions of photons with matter. MONACO uses the Evaluated Photon Data Library 97 (EPDL97)⁷, which is distributed together with the Geant4 library, as cross-section data of photoelectric absorption. In our physics implementation, a K-shell fluorescent photon is generated with a probability of a fluorescence yield just after the photoelectric absorption. Atomic properties relevant to the fluorescence, namely K-shell line energies, fluorescence yields, and $\text{K}\beta$ -to- $\text{K}\alpha$ ratios, are taken from Thompson et al. (2001), Krause (1979), and Ertuğral et al. (2007), respectively. $\text{K}\alpha_2$ -to- $\text{K}\alpha_1$ intensity ratios are fixed to 0.5. When an Auger electron is generated, tracking is stopped. Table 2 summarizes the energies of K-edge, K-lines, and the fluorescence yields used in our model.

Scattering by electrons also plays an important role in generating spectral features particularly at the hard X-ray band above 10 keV and the Compton shoulders of the iron K line at 6.4 keV. Since most electrons are bound to atoms or molecules in the condition of interest, photons are mostly scattered by electrons bound to hydrogen and helium. Binding an electron to an atom or molecule alters the scattering process, though many previous studies of the AGN reflection had considered only Compton scattering by free electrons at rest. The scattering process by a bound electron can be classified under three channels by difference in the final state of the target electron: (1) Rayleigh scattering to the ground state, (2) Raman scattering to excited states, and (3) Compton scattering to free states (Sunyaev & Churazov 1996). The shape of the Compton shoulder is greatly modified by the electron binding since the target electron is not at rest but has finite momentum in the atomic or molecular system. Thus, accurate treatment of the scattering process by a bound electron is of great importance in evaluating detailed spectral features measured by high-resolution spectroscopy. Details about the physics implementation are described in Odaka et al. (2011; see their Appendix).

2.3. Comparison with the MYTORUS Model

To demonstrate the performance of our simulation model generated by MONACO, we make a comparison with a widely used X-ray spectral model for AGN torus studies that is also based on Monte Carlo simulations. We select MYTORUS (Murphy & Yaqoob 2009) as a benchmark model since it assumes a simple, well-defined torus geometry with an opening

⁷ <https://www-nds.iaea.org/epdl97/>

Table 2
Energies of K-edge, K-lines, and Fluorescence Yields

Z^a	Element	K-edge ^b	$K\alpha_1^b$	$K\alpha_2^b$	$K\beta^b$	$Y_{K\alpha}^c$	$Y_{K\beta}^c$
1	H	13.6
2	He	23.4
3	Li	59.9	54.30
4	Be	118.4	108.50
5	B	195.6	183.30	0.0017	...
6	C	291.0	277.00	0.0028	...
7	N	404.9	392.40	0.0052	...
8	O	537.3	524.90	0.0083	...
9	F	688.4	676.80	0.0130	...
10	Ne	858.2	848.60	848.60	...	0.0180	...
11	Na	1064.0	1040.98	1040.98	1071.10	0.0230	...
12	Mg	1294.5	1253.60	1253.60	1302.20	0.0296	0.0004
13	Al	1549.9	1486.70	1486.27	1557.45	0.0382	0.0008
14	Si	1828.5	1739.98	1739.38	1835.94	0.0487	0.0013
15	P	2130.4	2013.70	2012.70	2139.10	0.0604	0.0026
16	S	2455.9	2307.84	2306.64	2464.04	0.0736	0.0044
17	Cl	2804.9	2622.39	2620.78	2815.60	0.0906	0.0063
18	Ar	3177.6	2957.70	2955.63	3190.50	0.1068	0.0112
19	K	3583.3	3313.80	3311.10	3589.60	0.1258	0.0142
20	Ca	4015.0	3691.68	3688.09	4012.70	0.1452	0.0178
21	Sc	4465.8	4090.60	4086.10	4460.50	0.1668	0.0212
22	Ti	4940.6	4510.84	4504.86	4931.81	0.1897	0.0243
23	V	5439.6	4952.20	4944.64	5427.29	0.2151	0.0278
24	Cr	5957.6	5414.72	5405.51	5946.71	0.2424	0.0325
25	Mn	6510.9	5898.75	5887.65	6490.45	0.2692	0.0388
26	Fe	7083.4	6403.84	6390.84	7057.98	0.3003	0.0398
27	Co	7680.7	6930.32	6915.30	7649.43	0.3275	0.0455
28	Ni	8302.8	7478.15	7460.89	8264.66	0.3583	0.0477
29	Cu	8943.2	8047.78	8027.83	8905.29	0.3873	0.0526
30	Zn	9622.4	8638.86	8615.78	9572.00	0.4166	0.0574

Notes.

^a Atomic number.

^b Energies in unit of eV.

^c Fluorescence yield of K lines.

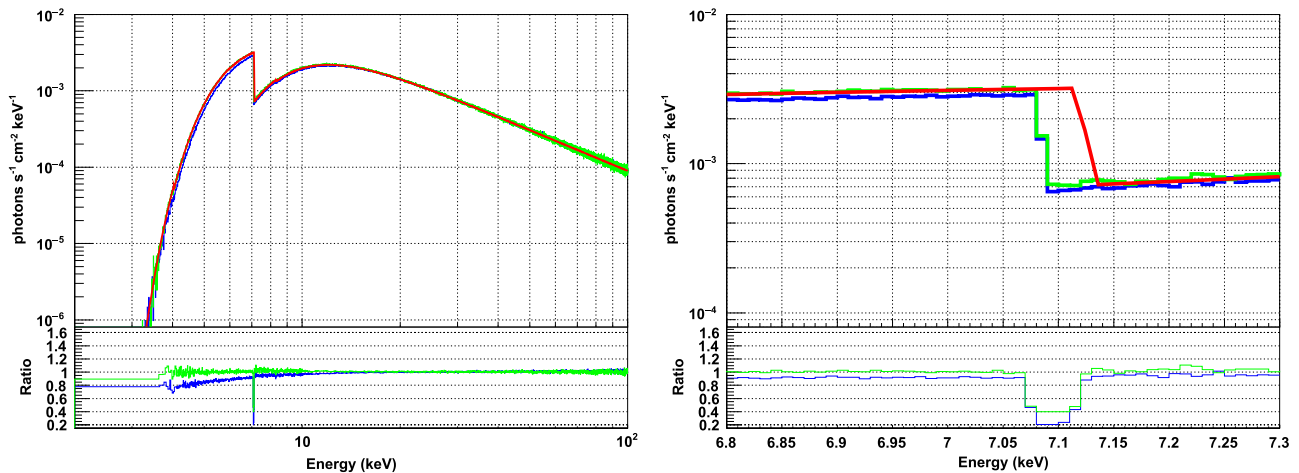


Figure 2. Spectra of the direct component for comparison between MONACO and MYTORUS. The left panel is shown in 2–100 keV while the right panel is enlarged around the iron K-shell edge at 7 keV. Three models are shown: the MYTORUS model (red), the free electron case generated with MONACO (green), and the bound electron case generated with MONACO (blue). (See the text for details). The bottom panels in each figure are spectral ratios against MYTORUS.

angle of 60° and a metal abundance of 1 solar value, where the solar values are based on Anders & Grevesse (1989). Then, we performed Monte Carlo simulations with MONACO to generate

a spectral model for parameters of $\theta_{OA} = 60^\circ$, $A_{\text{metal}} = 1.0$, and $N_{\text{H}} = 1 \times 10^{24} \text{ cm}^{-2}$. The initial spectrum is assumed to be a power law with a photon index of 1.9 in an energy range

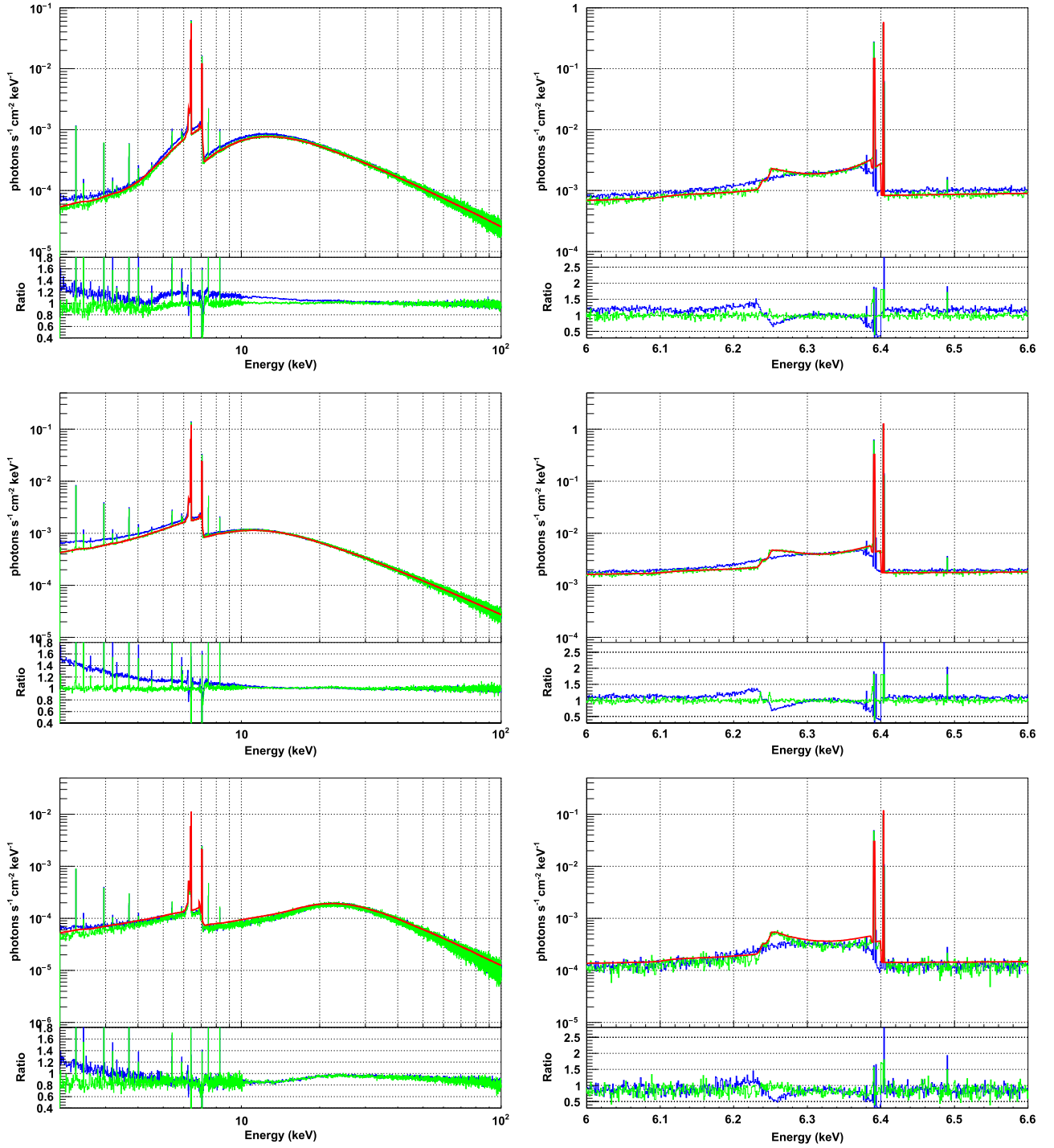


Figure 3. Spectra of the reprocessed component for comparison between `MONACO` and `MYTORUS`. The left panel is shown in 2–100 keV, while the right panel is enlarged around the iron $K\alpha$ line at 6.4 keV. Three models are shown: the `MYTORUS` model (red), the free electron case generated with `MONACO`, and the bound electron case generated with `MONACO` (blue). (See the text for details). The bottom panels in each figure are spectral ratios against `MYTORUS`. The top and middle panels are the comparison in the case of $0.1 \leq \cos \theta_i < 0.2$ (or $81^\circ 4 \pm 2.9$) and $0.6 \leq \cos \theta_i < 0.7$ (or $49^\circ 3 \pm 3.8$) for $N_{\text{H}} = 1 \times 10^{24} \text{ cm}^{-2}$, respectively, and the bottom panel is in the case of $N_{\text{H}} = 1 \times 10^{25} \text{ cm}^{-2}$ and $0.1 \leq \cos \theta_i < 0.2$.

of 2–300 keV, and 6.4×10^8 incident photons were simulated in total to make the spectrum.

The spectrum emerging from the AGN torus system can be divided into two components, namely direct component and reprocessed component. The direct component is composed of photons that are initially emitted at the central source and then escape from the system without any interaction. The

reprocessed component is a result of scattering and fluorescence following photoelectric absorption. Since `MONACO` is able to distinguish these two components for each observed photon and `MYTORUS` also provides the two components separately, we make the comparison between the two models for each component to demonstrate the effects of detailed implementations of the physical processes.

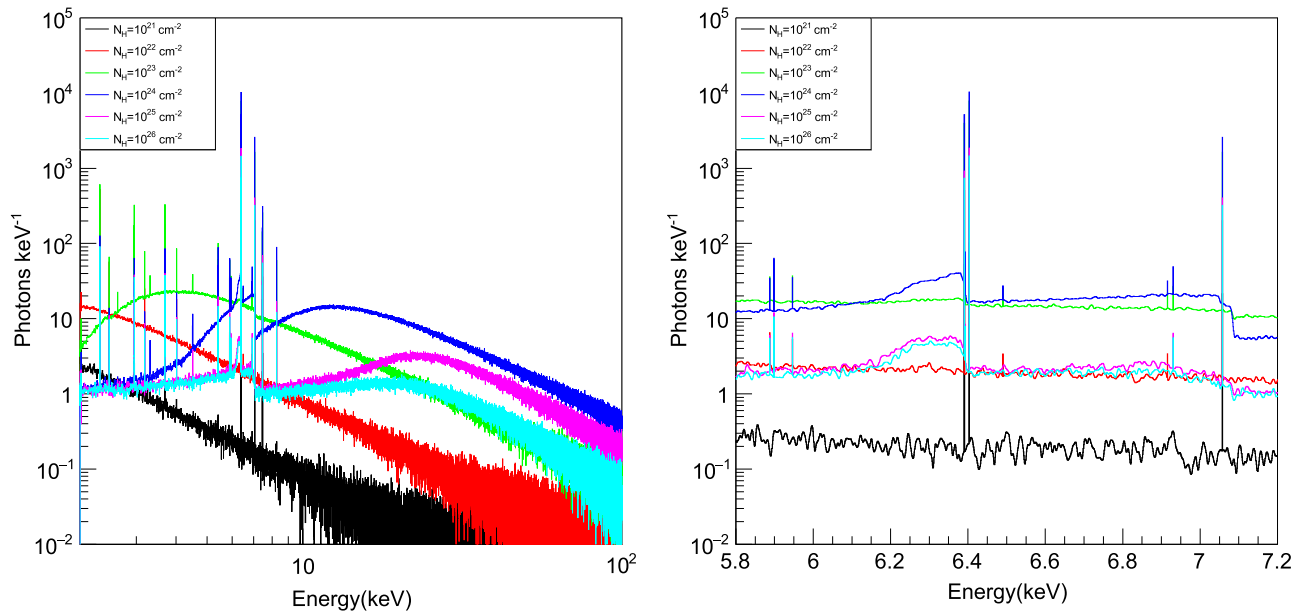


Figure 4. Spectra of the reprocessed component in the case of smooth torus with an inclination angle of $\theta_i = 0.1\text{--}0.2$, for various column densities $N = 10^{21}, 10^{22}, 10^{23}, 10^{24}, 10^{25}$, and 10^{26} cm^{-2} . The right panel is an enlargement around the Fe-K line.

In Figure 2, we show spectra of the direct component for comparison between MONACO and MYTORUS. These spectra are extracted by integrating escaping photons that are within $0.1 \leq \cos \theta_i < 0.2$ (or 81.4 ± 2.9). In this work, we assume that in the AGN torus all electrons responsible for scattering are bound to atoms or molecules, while MYTORUS uses Compton scattering by free electrons at rest. In order to check for consistency with MYTORUS, we compare three spectra: MYTORUS model spectrum, a MONACO spectrum assuming free electrons at rest, and a MONACO spectrum assuming electrons bound to hydrogen molecules and helium atoms. The comparison shows excellent agreement among the three models above 10 keV within 5%. In the low-energy band, our model of the bound electron case gives a less direct component, and this can be understood as described below for a similar comparison of the scattering component. Also, another difference can be seen in the enlarged view around the iron K-shell edge at 7 keV. The difference in energy of the iron edge comes from the difference in the origin of the cross-section data of photoelectric absorption used in the two models. The MONACO spectrum of the bound electron scattering shows slightly lower than that of the free electron scattering since a cross section of Rayleigh scattering is enhanced by a factor of two for a hydrogen molecule, resulting in an insignificant reduction of the direct component. Note that this direct component is easily calculated by the total cross section (absorption and scattering), which means that we do not need detailed Monte Carlo simulations in practice. MYTORUS actually provides the direct component model without Monte Carlo simulations. Here we have verified the Monte Carlo simulations in MONACO by using the direct component, which is easily calculated.

Then, we compare the reprocessed component, which is best calculated by accurate Monte Carlo simulations. Figure 3 shows the spectra of the reprocessed component given by the

three different models. These spectra are extracted by integrating escaping photons that have direction within $0.1 \leq \cos \theta_i < 0.2$ (or 81.4 ± 2.9) and $0.6 \leq \cos \theta_i < 0.7$ (or 49.3 ± 3.8). Also, the comparison in the case of $N_H = 1 \times 10^{25} \text{ cm}^{-2}$ and $0.1 \leq \cos \theta_i < 0.2$ are shown. Again, we can see excellent agreement among them in the broad-band view while the MONACO spectra display fluorescent lines of all abundant elements in addition to iron. The MONACO spectrum of the bound electron scattering shows higher than the other spectra at the lower energy band below 20 keV. This is also because of the enhancement of Rayleigh scattering, showing consistency with the reduction seen in the direct component.

An interesting difference in the spectral shape appears in the Compton shoulder associated with the iron $K\alpha$ line, as shown in the right panels of Figure 3. The MONACO spectrum of the free electron scattering perfectly agrees with MYTORUS, simply because the physical conditions assumed in the two models are completely identical. The bound electron case, however, shows a different profile of the Compton shoulder particularly at the low-energy edge of the shoulder at 6.24 keV, which corresponds to the maximum energy transfer to the recoil electron (i.e., at the scattering angle of 180° with respect to the incident direction). While the case of free electrons at rest shows a sharp edge at 6.24 keV, atomic or molecular binding smears the Compton shoulder profile. This is a result of non-zero momentum of the target electron bound to an atom or molecule, which broadens the energy distribution of the scattered photon. This effect by electron binding is quite similar to what we would see if free electrons had thermal motion in a plasma (see, e.g., Sunyaev & Churazov 1998). It is essential to treat scattering by bound electrons for high-resolution spectroscopy to evaluate the Compton shoulder seen in the AGN reflection.

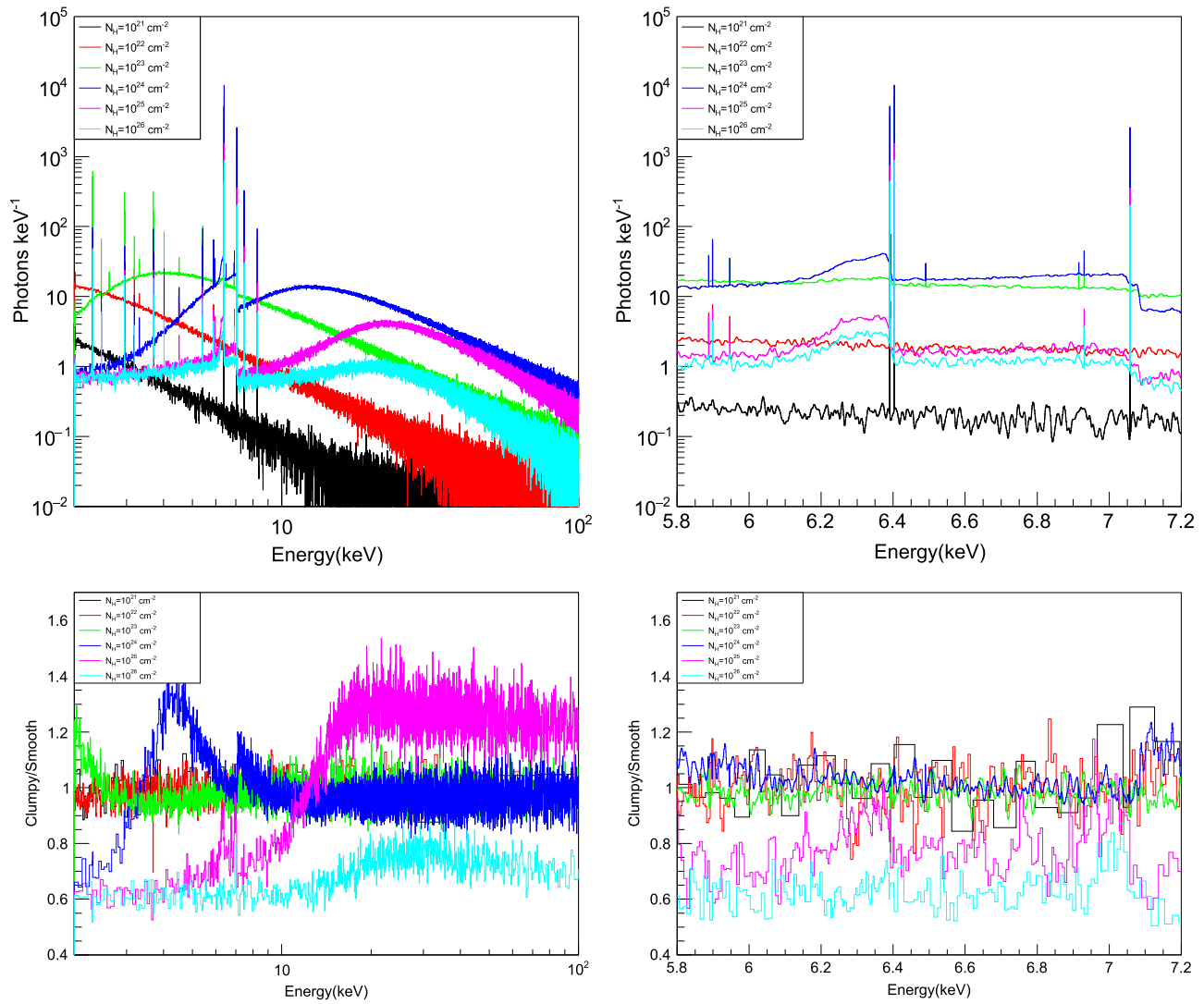


Figure 5. (Top) Spectra of the reprocessed component in the case of a clumpy torus, for various column densities $N = 10^{21}, 10^{22}, 10^{23}, 10^{24}, 10^{25}$, and 10^{26} cm^{-2} . The right panel is an enlargement around the Fe-K line. (Bottom) Spectral ratios of clumpy to smooth tori for the reprocessed components.

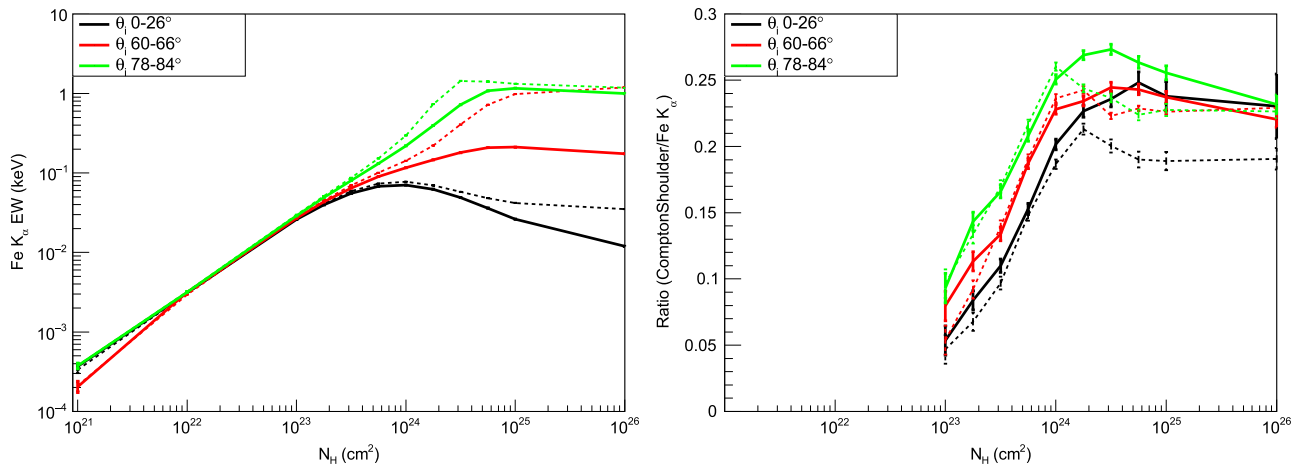


Figure 6. Left panel is a Fe-K line (core plus Compton shoulder) equivalent width (EW) against the column density N_{H} for three inclination angles. The right panel is a flux ratio of Fe-K Compton shoulder to line core against N_{H} . Solid and dashed lines represent clumpy and smooth tori, respectively.

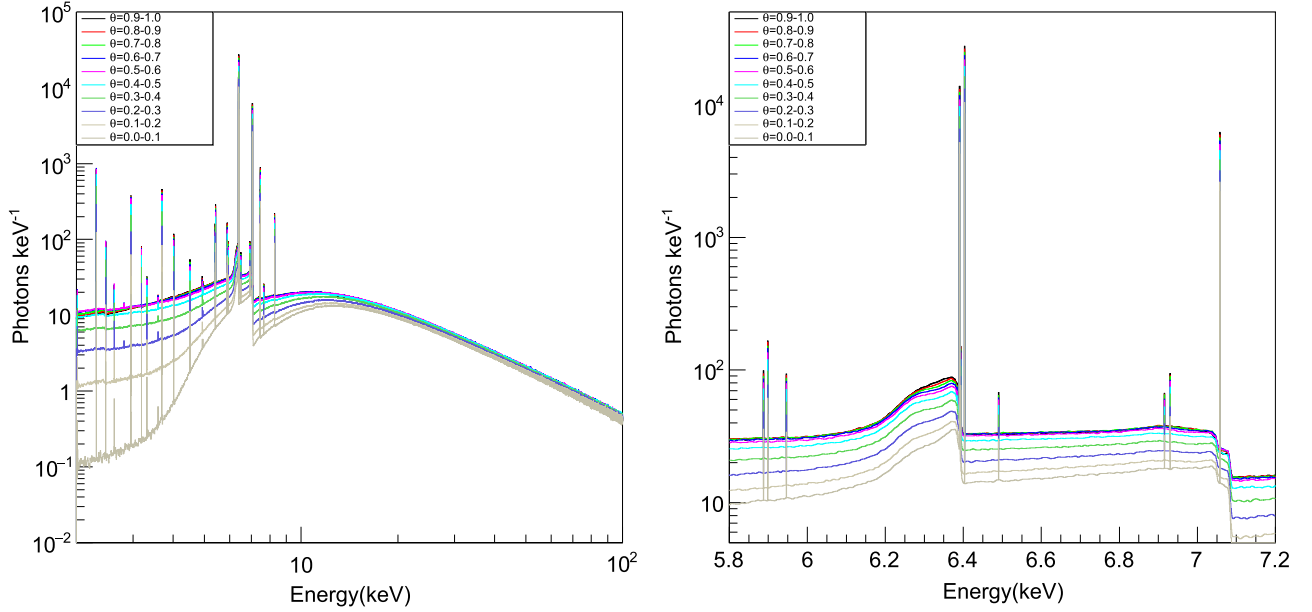


Figure 7. Spectra of the reprocessed component in the case of a smooth torus with a column density of $N_{\text{H}} = 10^{24} \text{ cm}^{-2}$, for various inclination angles $\cos \theta_i = 0.9\text{--}1.0, 0.8\text{--}0.9,$ and $0\text{--}0.1$ from top to bottom. The right panel is an enlargement around the Fe–K line.

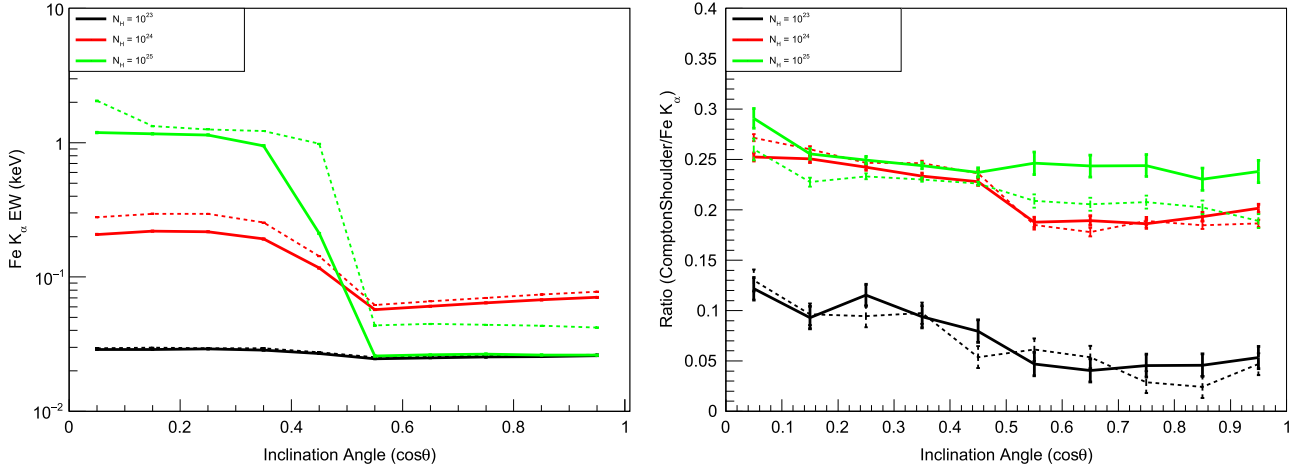


Figure 8. The left panel is a Fe–K line (core plus Compton shoulder) equivalent width (EW) against the cosine of the inclination angle θ_i for three column densities. The right panel is a flux ratio of the Fe–K Compton shoulder to the line core against $\cos \theta_i$. Dashed and solid lines correspond to the smooth and clumpy tori, respectively.

3. RESULTS

Here, we present X-ray spectra simulated by MONACO for an AGN torus in smooth and clumpy cases, together with behaviors of Compton shoulder of Fe–K α line, for various torus conditions. We represent an intrinsic spectrum by a power-law shape with a photon index 1.9 in the range of 2–300 keV, and generated a total number of 10^9 photons for each run. These photons were emitted in any direction within a 4π solid angle from the center isotropically. The abundance is referred to by Anders & Grevesse (1989), and hydrogen and helium in the torus are assumed to exist as molecules and atoms, respectively. We sorted the photons going out of the torus into 20 bins evenly spaced in the cosine of inclination angles in the range of $-1 \leq \cos \theta_i \leq +1$, where θ_i is the angle between the direction of photon and the z -axis. In this section, if we do not specify torus parameters

explicitly, we display X-ray reflection spectra with a condition of $0.1 \leq \cos \theta_i \leq 0.2$ ($\theta_i = 78.46 - 84.26$), $N_{\text{H}} = 10^{24} \text{ cm}^{-2}$, $\theta_{\text{OA}} = 60^\circ$, $A_{\text{metal}} = 1.0$ solar, and $V_{\text{turb}} = 0 \text{ km s}^{-1}$. Namely, this fiducial parameter set represents a nearly edge-on view of a torus. We studied the dependences on the column density for both of smooth and clumpy cases, on the inclination and metal abundance for the smooth case, and on the volume filling factor and clump radius for the clumpy case.

Since simulation spectra have Poisson noise especially in the high-energy band, we created the simulated spectra with 1 eV bin, and then smoothed by a running average with 41 bins in $E \leq 8 \text{ keV}$ or $41 + 2\sqrt{(E(\text{keV}) - 8)/0.05}$ bins in $E > 8 \text{ keV}$, where E is the photon energy. In this case, the smoothing procedure was applied only for the continuum by excluding the line region. Then, the number of energy bins is 298,000.

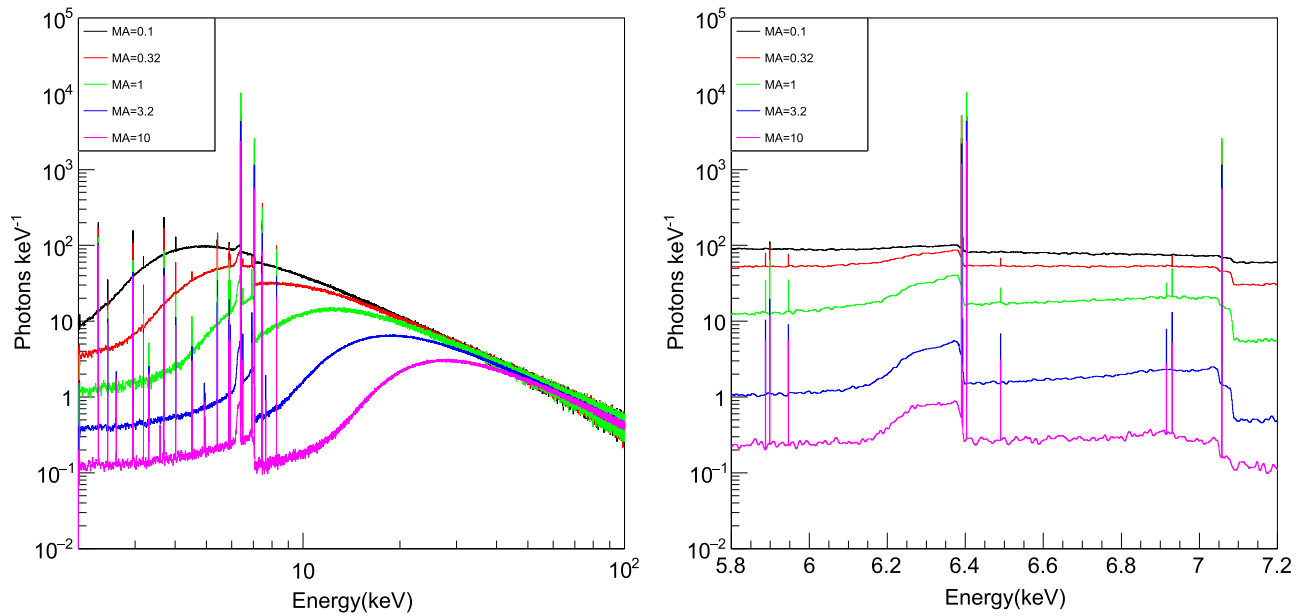


Figure 9. Spectra of the reprocessed component in the case of a smooth torus with $N_{\text{H}} = 10^{24} \text{ cm}^{-2}$ and $\cos \theta_i = 0.1\text{--}0.2$, for various metal abundances (MA) in solar units. The right panel is an enlargement around the Fe-K line.

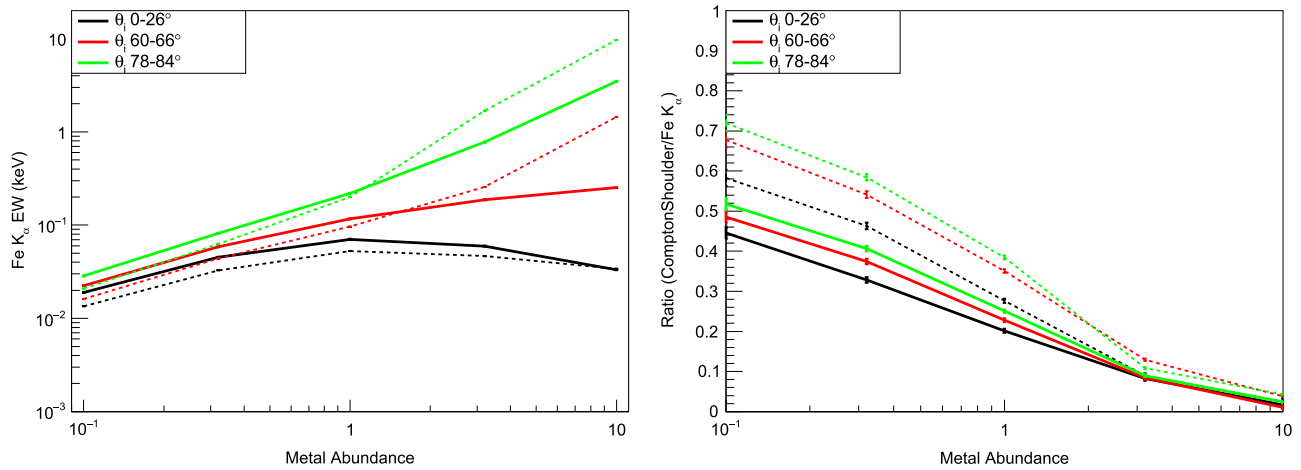


Figure 10. The left panel is a Fe-K line (core plus Compton shoulder) equivalent width (EW) against the metal abundance for three inclination angles. The right panel is a flux ratio of the Fe-K Compton shoulder to the line core against the metal abundance. Both panels are in the case of $N_{\text{H}} = 10^{24} \text{ cm}^{-2}$. Dashed and solid lines correspond to the smooth and clumpy torus cases, respectively.

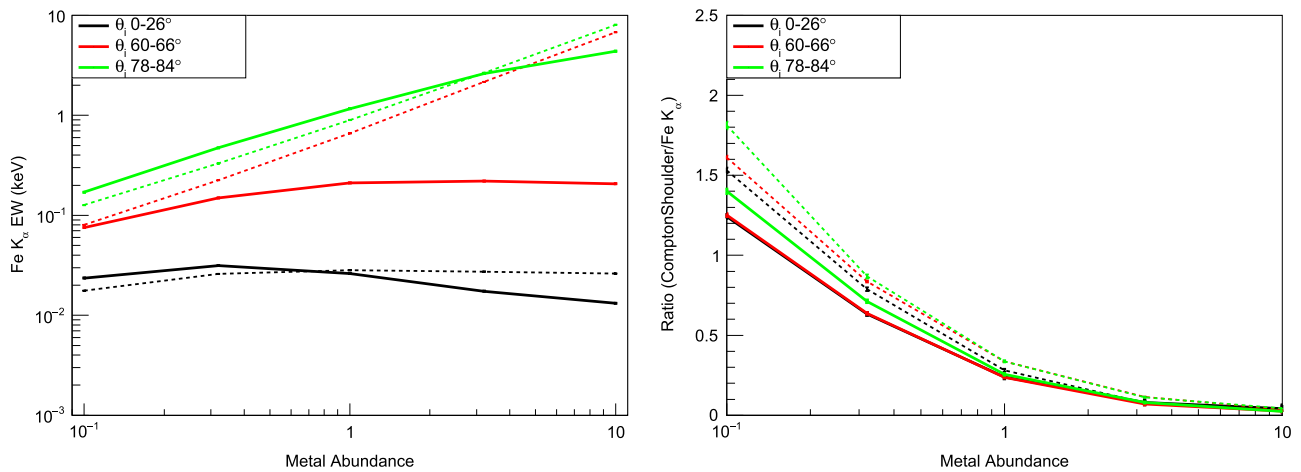


Figure 11. Same as Figure 10, but in the case of $N_{\text{H}} = 10^{25} \text{ cm}^{-2}$.

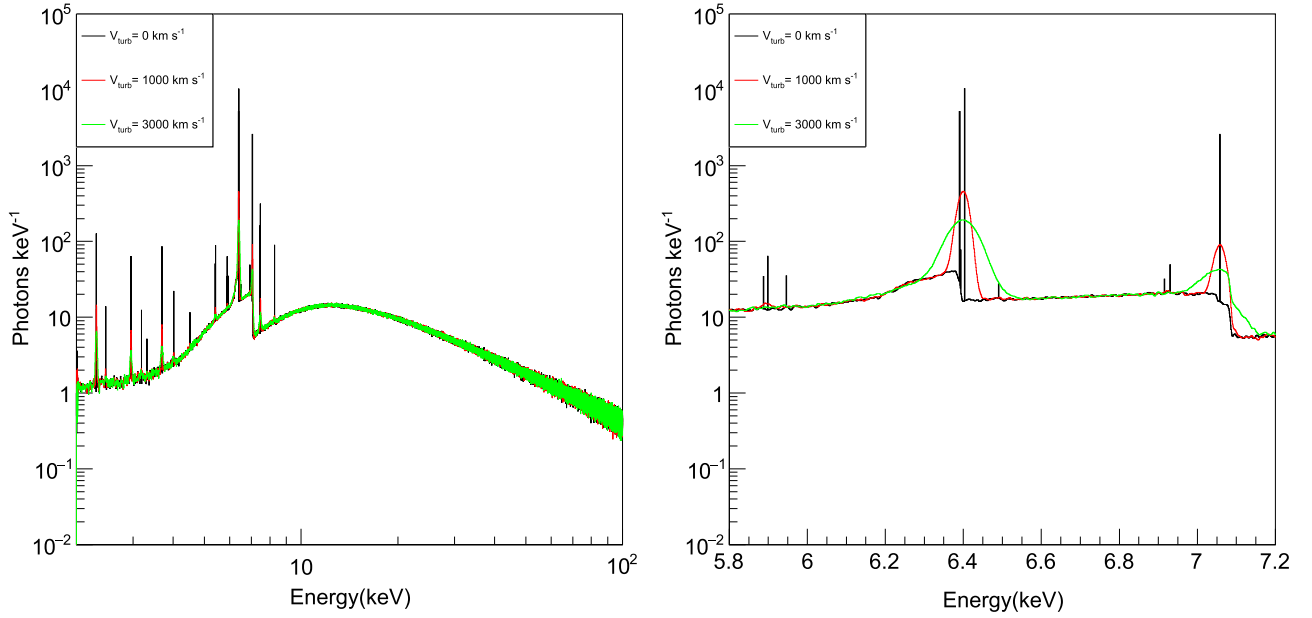


Figure 12. Spectra of the reprocessed component in the case of a smooth torus with $\cos \theta_i = 0.1-0.2$, for various turbulence velocities. The right panel is an enlargement around the Fe-K line.

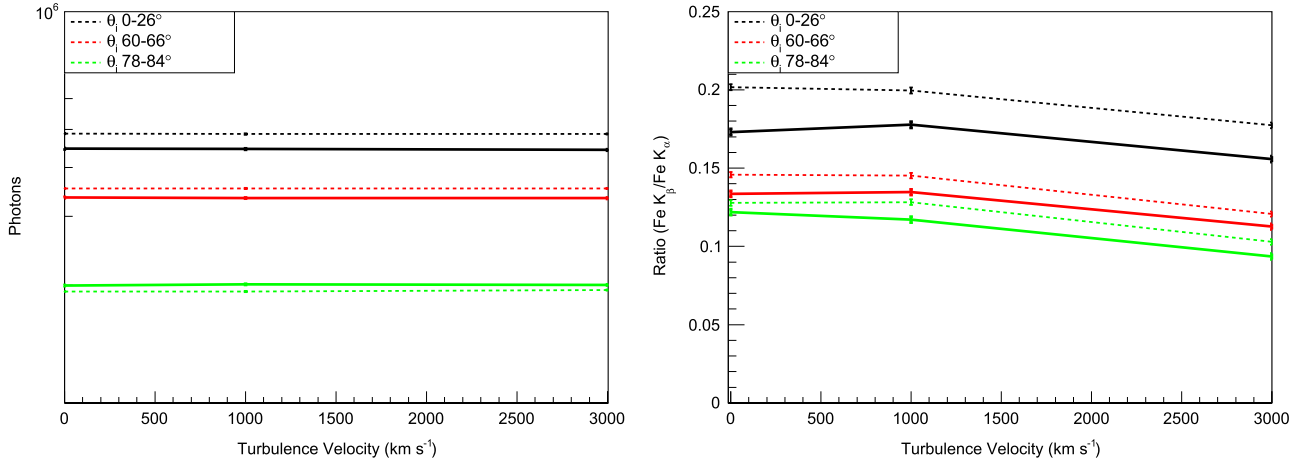


Figure 13. The left panel is a Fe-K line (core plus Compton shoulder) equivalent width (EW) against the turbulence velocity for three inclination angles. The right panel is a flux ratio of Fe-K β to Fe-K α against the turbulence velocity. Dashed and solid lines correspond to the smooth and torus cases, respectively.

3.1. Dependence of Hydrogen Column Density (Smooth, Clumpy)

At first, we studied the dependence on the hydrogen column density N_H of the torus in the range of $10^{21}-10^{26} \text{ cm}^{-2}$. The simulated spectra of the reprocessed component in 2–10 keV are shown in Figure 4. The spectral shape is almost identical to the intrinsic one at low N_H and the flux is almost proportional to N_H ; scattering occurs in proportion to N_H , and scattered photons mostly escape out of the torus without absorption in such a Compton-thin regime. Around $N_H = 10^{23-24} \text{ cm}^{-2}$, the low-energy part becomes attenuated and the flux in the high-energy part does not increase as N_H becomes larger. At the Compton-thick regime of $N_H > 10^{24} \text{ cm}^{-2}$, the flux at the high-energy part decreases due

to the effect of multi-scattering. This behavior in the Compton-thick regime is also reported in Ikeda et al. (2009) and Murphy & Yaqoob (2009).

The right panel of Figure 4 shows the spectra around the Fe-K lines. We can see a change of shape and strength of the Compton shoulder against N_H . The Compton shoulder becomes more apparent for larger N_H . The Compton shoulder monotonically decreases toward the lower energy at $N_H < 10^{24.5} \text{ cm}^{-2}$, while an edge-like structure at 6.3 keV becomes prominent at the Compton-thick regime. This behavior can be understood as follows. In Figure 19, we summarize the map of locations at which the last interaction between photons and torus for various simulation conditions and photon energies. Looking at these figures, it is found that,

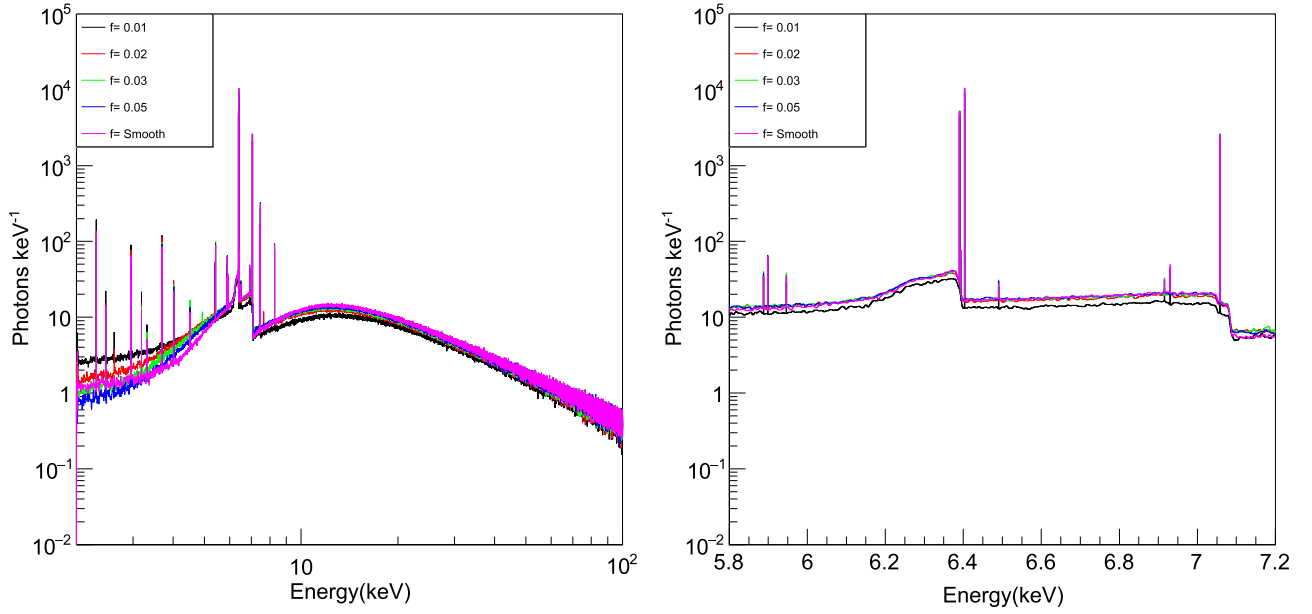


Figure 14. Spectra of the reprocessed component in the case of a clumpy torus for various volume filling factor f . The right panel is an enlargement around the Fe-K line.

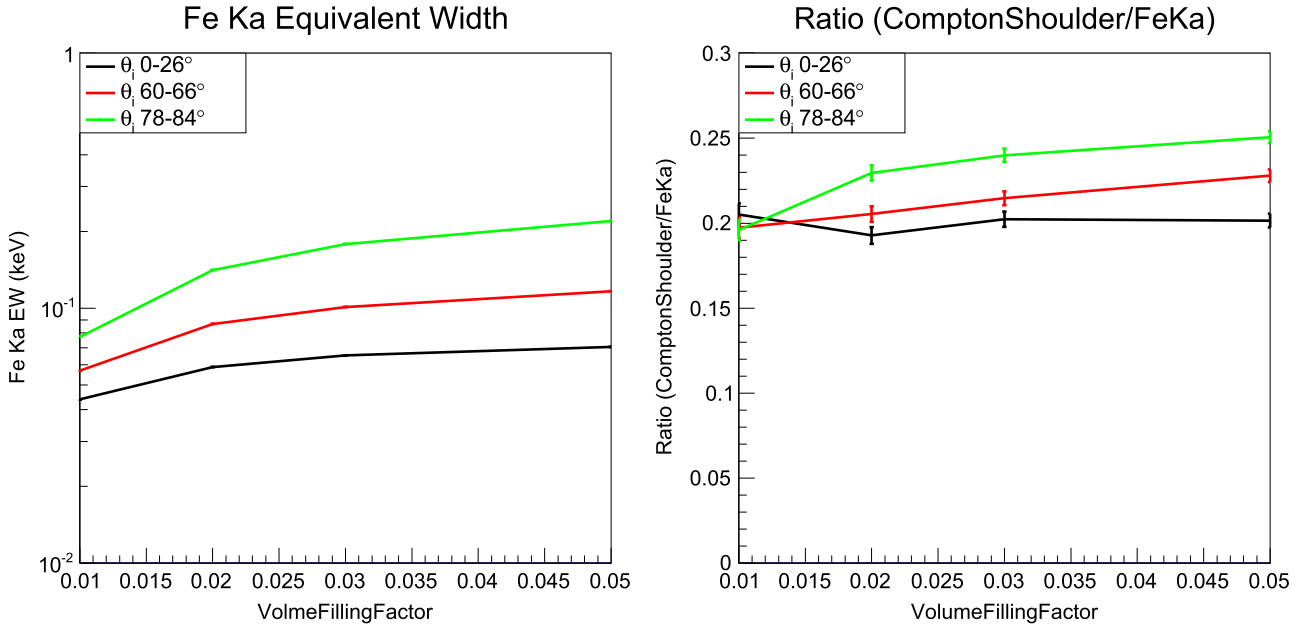


Figure 15. Left panel is a Fe-K line (core plus Compton shoulder) equivalent width (EW) against the volume filling factor with $\theta_i = 0.1-0.2$. The right panel is a flux ratio of Fe-K Compton shoulder to line core against the volume filling factor for three inclination angles. Both panels are in the case of a clumpy torus.

at $N_{\text{H}} < 10^{24} \text{ cm}^{-2}$, photons in the Compton shoulder come from the whole torus region with a wide range of scattering angles, leading to a wide range of photon energies after Compton scattering. At the Compton-thick regime, most of the scattered photons come from the torus behind the central engine with a large scattering angle toward the observer and a large Compton loss, and thus the fraction of photons close to 6.4 keV decreases.

For the clumpy torus, we set a volume filling factor $f = 0.05$ and a clump radius $aR_{\text{torus}} = 0.005R_{\text{torus}}$. Figure 5 (top) shows the N_{H} -dependence of reflection spectra in the case of the

clumpy torus, and Figure 5 (bottom) shows spectral ratios of clumpy to smooth tori. For the viewing angle of $\cos \theta_i = 0.1-0.2$, the spectral shape is somewhat different from that of the smooth torus, as seen in the spectral ratio of clumpy to smooth tori. As N_{H} increases, a part of the spectrum becomes humped in the clumpy torus case and the hump moves to the higher energy. From the lower energy part, the flux ratio (for the clumpy torus compared with the smooth case) becomes smaller, and at last the ratio becomes almost constant at ~ 0.6 at $N_{\text{H}} = 10^{26} \text{ cm}^{-2}$ for the clumpy torus than that for the smooth case. As shown in the Appendix (Figures 20–22), the flux of

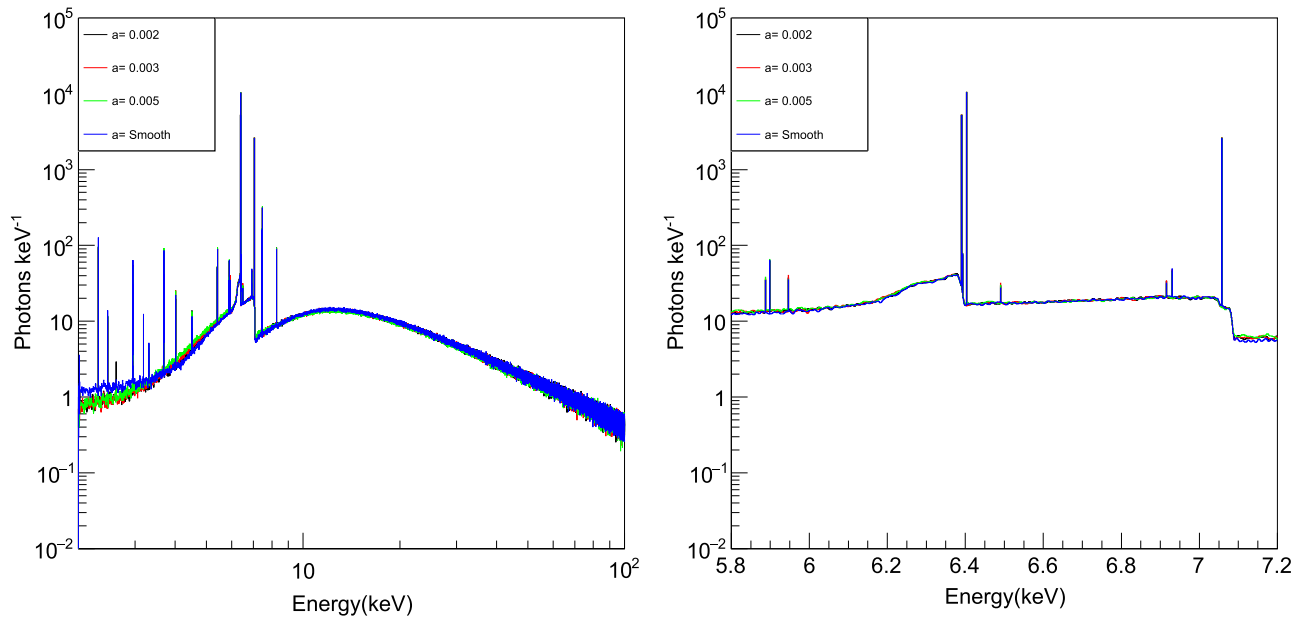


Figure 16. Spectra of the reprocessed component in the case of the clumpy torus for various clump radii a with $\cos \theta_i = 0.1-0.2$. The right panel is an enlargement around the Fe-K line.

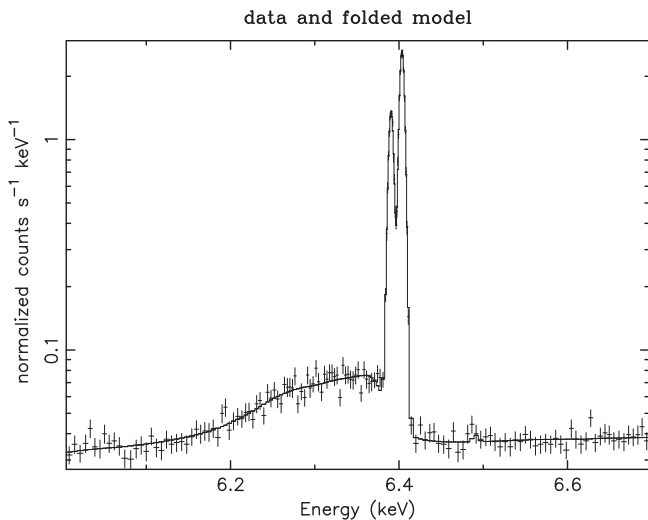


Figure 17. Simulated *ASTRO-H/SXS* spectra for Mrk 3 around the Fe-K line (6.0–6.7 keV), based on our clumpy torus model. The solid line represents the best-fit model. See the detail in the text.

reprocessed components for the clumpy torus is lower than that for the smooth torus at most inclination angles, except the edge-on ($\cos \theta_i = 0-0.1$), in the case of $N_H = 10^{26} \text{ cm}^{-2}$. This behavior is also reported by Liu & Li (2014); note that the average number of clumps toward the equatorial direction in our case is 7.5 (Section 2.1). Since the density of each clump is f^{-1} times as high as the average density in the smooth torus case, an effective optical depth is larger and thus the flux becomes lower. The shape of Compton shoulder is also similar but photons close to the line core are somewhat more numerous in the clumpy torus at $N_H = 10^{25} \text{ cm}^{-2}$, due to the fact that photons scattered at the front of the central engine with a small scattering-angle leak to the line of sight more easily in the clumpy torus than in the smooth torus around this N_H .

The dashed line in the left panel of Figure 6 shows the equivalent width (EW) of the Fe-K α line (core plus Compton shoulder); EW is the ratio relative to the sum of the reflection and the direct continuum. This result is consistent with previous studies (Ikeda et al. 2009; Murphy & Yaqoob 2009). The dashed line in the right panel of Figure 6 shows an integrated flux ratio of the Compton shoulder to the line core. The flux of the Compton shoulder is derived by subtracting the continuum estimated in the wider energy bands adjacent to the line core and the shoulder. The fraction of the Compton shoulder increases with the column density N_H in the Compton-thin regime, and saturates at 0.2–0.25 in the Compton-thick regime. This behavior is similar to that in Matt (2002), and reasonably understood as follows. There is a peak at $N_H = 10^{24} \text{ cm}^{-2}$, the fraction decrease just above the peaking column density is thought to be due to the difference of the effective optical depth between line core photons and Compton shoulder photons. The former has one interaction in the torus, while the latter has multiple interactions and thus a larger effective optical depth than the former. Therefore, the Compton shoulder becomes prominent faster than the line core at a low N_H and its flux decreases faster than the core flux at a high N_H . Then, the ratio of the Compton shoulder to the line core has a peak between the two regimes.

The solid lines in the two panels of Figure 6 represent the behavior in the case of the clumpy torus. The dependence of the EW and the fraction of the Compton shoulder against N_H is different from those of the smooth torus. The difference of the EW is, however, not large enough for us to be able to distinguish clearly through observations. On the other hand, a fraction of the Compton shoulder is larger by several tens of percent in the Compton-thick regime for the clumpy torus, compared with the smooth one. This is explained in such a way that the Compton shoulder events that experience multiple interactions could escape from the torus easier in the clumpy torus than in the smooth torus due to intraclump spaces.

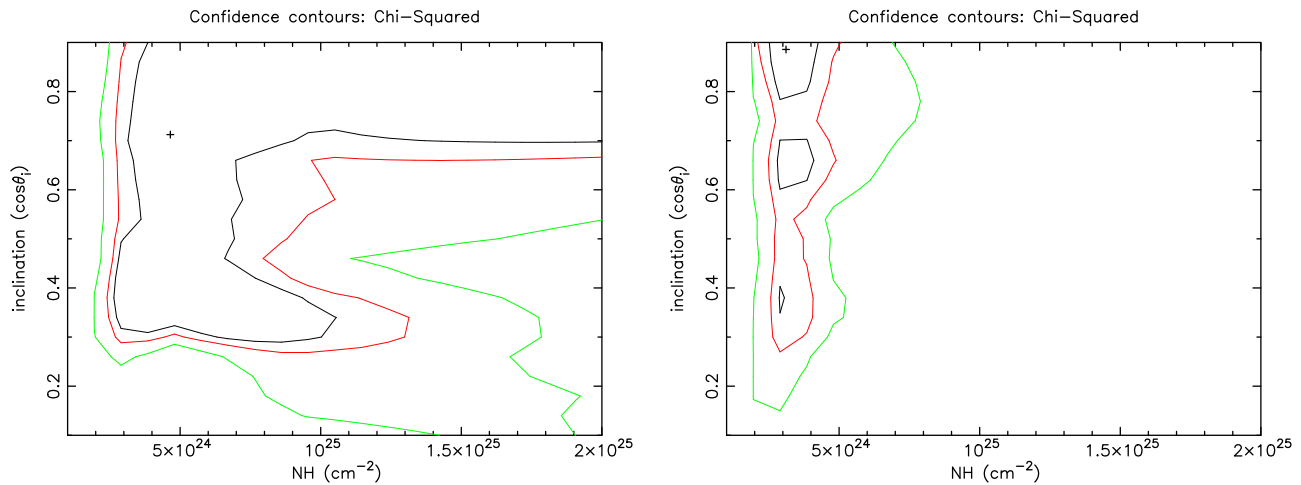


Figure 18. Confidence contours between column density and inclination angle for spectral fitting of the simulated *ASTRO-H*/SXS spectrum only around the Fe–K line. Black, red, and green lines represent 68%, 90%, and 99% confidence levels, respectively. See the text for details. The left and right panels are for the smooth and clumpy cases, respectively. “+” represents a location of the best-fit values.

3.2. Dependence of Inclination Angle (Smooth, Clumpy)

Figure 7 shows the simulated reprocessed spectra for $\cos \theta_i = 0-1$ in steps of 0.1 in case of $N_H = 10^{24} \text{ cm}^{-2}$ for the smooth torus. To create this plot, we generate a total number of 10^{10} photons for a run, in order to keep the statistics for various inclination angles. In the left panel of this figure, the spectral shape and flux are almost identical in high-energy band for any inclination angle, since the absorption effect is negligible and scatterings occur with various angles at various positions to reduce the scattering-angle dependence. In the lower energy band, the flux decreases for the larger inclination angle due to the absorption. The shape of the Compton shoulder becomes more upwardly concave at the smaller inclination angle. At $\cos \theta_i = 0.5-0.9$ (θ_i is small), the last scattering position of photons in the Fe–K region includes the equatorial region of the torus behind the central engine from the observer, and the Compton shoulder events scattered in such a region have a large scattering optical depth and thus a lower energy of scattered photons due to Compton loss. At larger inclination angle with $\cos \theta_i < 0.5$, the equatorial region of the torus behind the central engine cannot be observed from the observer, and thus the Compton shoulder events with lower energy decrease.

Figure 8 shows the inclination angle dependence of the Fe–K line EW and the Compton shoulder to the line core ratio for three cases with $N_H = 10^{23}$, 10^{24} , and 10^{25} cm^{-2} . This figure shows results for both smooth and clumpy cases. The inclination angle of the EW jump corresponds to the boundary whether the line from the center to the observer passes the torus or not. This behavior is consistent with that of Murphy & Yaqoob (2009). The fraction of the Compton shoulder increases with the inclination angle (i.e., with smaller $\cos \theta_i$ values). For a larger N_H , the fraction is larger for the clumpy torus than the smooth one, as seen in the N_H dependence.

3.3. Dependence of Metal Abundance (Smooth, Clumpy)

So far we have performed a simulation under the condition that metal abundance is the same as the solar system. In this subsection, we studied the dependence on metal abundance.

Table 3

Model Parameters for *ASTRO-H* SXS Simulation for the XSPEC Model:
Phabs*(Powerlaw + Zvphabs*Powerlaw + Reflection)

Component	Parameter	Unit	Value
zvphabs	nH	10^{22} cm^{-2}	8.7×10^{-2}
powerlaw	Index	...	1.8
powerlaw	norm	...	1.27×10^{-4}
phabs	nH	10^{22} cm^{-2}	110
powerlaw ^a	Index	...	1.8
powerlaw	norm	...	5×10^{-3}
Reflection	NH	10^{22} cm^{-2}	3×10^{24}
Reflection	Inclination $\cos \theta_i$...	0.5
Reflection	Metal Abundance	solar	1.0
Reflection	Turbulence Velocity	km s^{-1}	0
Reflection	Volume Filling Factor	...	0.005

Note.

^a Normalization in units of $\text{photons cm}^{-2} \text{ s}^{-1} \text{ keV}^{-2}$ at 1 keV.

Figure 9 shows the reprocessed spectra on various metal abundances with $N_H = 10^{24} \text{ cm}^{-2}$ for the smooth torus. Metal abundances of heavy elements are kept to follow the solar abundance ratio. For this plot, we generate a total number of 10^{10} photons for $A_{\text{metal}} = 3.2$ or 10 in order to keep the statistics, but 10^9 photons for other A_{metal} values. Metal abundance dependence on the reprocessed spectra is similar to that on N_H , but the difference is that a scattered component in the lower energy part is weak and there is no flux change in the higher energy band. This is due to the fact that the amount of hydrogen in the main scattering atoms does not change in this case.

Figures 10 and 11 show the EW and the fraction of the Compton shoulder to the line core as a function of metal abundance for three inclination angles. We show two cases of $N_H = 10^{24} \text{ cm}^{-2}$ and 10^{25} cm^{-2} for both smooth and clumpy cases. At large inclination angles, the EW increases with the metal abundance quasi-proportionally. Looking at the Fe–K line core flux and continuum, this increase is not due to the line

flux increase but due to the continuum reduction at high metal abundances. At the small inclination angle, EW does not increase with the metal abundance since the continuum reduction is weak. Interestingly, the fraction of the Compton shoulder to the line core is smaller at higher metal abundance. From the spectra in Figure 9, the flux of Compton shoulder becomes more heavily reduced than the line core flux at higher metal abundance. At higher metal abundance, the Compton shoulder events that run a longer path than the line core events in the torus are more strongly absorbed and the flux reduction is large.

For lower metal abundances, the clumpy case gives a higher EW and a lower Compton shoulder to line core ratio than the smooth case. On the other hand, for higher metal abundances, it gives a lower EW. The density in the clumpy case is higher than that in the smooth case with the same N_{H} in our definition. Consider a torus size R_{torus} , a clump size $aR_{\text{torus}} = 0.005R_{\text{torus}}$, and a mean free path $l_{\text{Fe}} = 0.035A_{\text{metal}}^{-1}R_{\text{torus}}$ at the Fe–K α line energy 6.4 keV under the metal abundance A_{metal} and the volume filling factor $f = 0.05$. The last one is derived by using the relation between N_{H} and the hydrogen number density n_{H} in Section 2.1. In the lower metal abundances, a mean free path l_{Fe} is larger than a clump size aR_{torus} but smaller than a torus size R_{torus} . For the clumpy torus, X-rays can efficiently pass through the intracomp space from the central source to the torus, generate the Fe–K lines almost everywhere in each torus, and then efficiently escape out of the torus. In other words, an effective volume to generate K α line photons is larger for the clumpy torus, and thus EW is larger and the Compton shoulder to line core ratio is smaller. For higher metal abundances, l_{Fe} becomes comparable to or smaller than the clump size aR_{torus} . In this case, l_{Fe} of the clumpy torus is smaller than that of the smooth torus by a factor of f due to higher density. Observed K α line photons come from the region within l_{Fe} of the surface of smooth torus or each clump. As a result, the effective volume to generate K α line photons is smaller for the clumpy torus, and thus the EW is smaller. In addition, the scattering efficiency of Fe–K α photons also becomes higher for the clumpy case, and the Compton shoulder to line core ratio is similar to that of the smooth torus.

3.4. Dependence of Turbulent Velocity (Smooth, Clumpy)

The matter in the torus might have a Keplerian and random velocity, but here we artificially give a random motion. Figure 12 shows the simulated reprocessed spectra for three v_{turb} for the smooth torus. Fe–K line width is certainly broadened, and the interesting feature is that a part of broadening K β line exceeds the absorption edge energy at 7.112 keV (X-ray Transition Energy Database).⁸ We can see this fact quantitatively in the K β to K α line ratio in Figure 13. This ratio decreases toward a high random velocity. Of course, this behavior could be dependent on the velocity field. In other words, we can extract the information of the velocity field in the torus from the K β to K α line ratio.

Figure 13 shows that the K β to K α line ratio of the clumpy torus is systematically smaller than that of the smooth one for any velocity dispersion; this difference is due to the difference of torus structure, smooth or clumpy. The difference is more prominent for a small inclination angle. It is found that the line intensity ratio of clumpy to smooth tori is smaller for the K β

line than for the K α line. This could be explained as follows. Contrary to the smooth case, where line photons that escaped from the torus can be directly observed, line photons that escaped from one clump are absorbed or scattered by front clumps before being observed. As a result, the line intensity of the clumpy torus becomes smaller than that of the smooth one. For a smooth torus, the observed line photons are generated mainly at the surface region with a thickness l_{Fe} . In this case, K β photons can escape more efficiently than K α photons. On the other hand, for a clumpy torus, the generated K α line photons can escape as efficiently as the K β photons, since a clump size aR_{torus} is smaller than a mean free path l_{Fe} . Then, the K β to K α line ratio becomes relatively smaller in the clumpy torus.

3.5. Dependence of Volume Filling Factor and Radius of Clumps (Clumpy)

We studied the dependence of the volume filling factor under the condition that the total N_{H} at the torus midplane is fixed to be 10^{24} cm^{-2} and the clump radius is fixed to $aR_{\text{torus}} = 0.005R_{\text{torus}}$. Accordingly, the number of clumps is proportional to the volume filling factor f while the column density of each clump is inversely proportional. Figure 14 shows the reprocessed spectra. We see a difference among spectra in the low and high energy. In the high energy, the flux is smaller for a smaller f , due to a lower scattering efficiency in the torus. On the other hand, in the low energy; the flux is higher for a smaller f since the scattered low-energy photons can easily escape from the torus for a small f . On the other hand, the shape of Compton shoulder is almost identical among different f . We also show the case of the smooth torus for reference, but the shape is almost the same. Quantitatively, as shown in Figure 15, there is only a weak dependence on f for the EW and the Compton shoulder fraction.

We next varied a clump radius aR_{torus} as $a = 0.005, 0.003,$ and 0.002 under the condition that the total N_{H} at the torus midplane and the volume filling factor f are constant at 10^{24} cm^{-2} and 0.05 , respectively. Then, the number of clumps in the torus varies as $\propto a^{-3}$. As shown in Figure 16, the reprocessed spectra at higher energy bands are almost identical except for the lowest energy part. As a result, we do not see any dependence on the clump radius for the EW and the fraction of Compton shoulder.

4. DISCUSSION

ASTRO-H/SXS (Takahashi et al. 2014) will for the first time enable us to perform unprecedentedly fine spectroscopy around the Fe–K line. Compton shoulder and absorption edge structures of the reflection component are interesting and important targets for SXS. *Chandra*/HETG has resolved the Compton shoulder clearly for X-ray binaries (Watanabe et al. 2003; Torrejón et al. 2010). On the other hand, the Compton shoulder was marginally resolved with HETG for the Seyfert 2 NGC 3783 (Kaspi et al. 2002; Yaqoob et al. 2005) with a very long exposure of 800–900 ks, and for the Seyfert 2 galaxy NGC 4507 with an exposure of 140 ks but with a low significance (Matt et al. 2004). Therefore, SXS will open a new window of Fe–K line spectroscopy with the Compton shoulder for AGNs with a normal exposure.

Here we demonstrate simulated spectra of SXS with our constructed X-ray reflection simulator. Models and parameters

⁸ <http://www.nist.gov/physlab/data/xraytrans/index.cfm>

of simulated spectra are based on the *Suzaku* observation of a Compton-thick Seyfert 2 galaxy Mrk 3 (Awaki et al. 2008). We model the AGN spectrum with the model `phabs*(powerlaw + zvphabs*powerlaw + reflection)` in the XSPEC model. Here, the `reflection` is a table model for a clumpy torus, generated by our AGN X-ray reflection simulator. Table 3 summarizes the model parameters. In this case, the X-ray flux in 2–10 keV is $8 \times 10^{-12} \text{ erg cm}^{-2} \text{ s}^{-1}$. We simulated the SXS spectrum with 500 ks exposure, by using SXS response matrices.

Since the advantage of SXS spectroscopic power is to resolve the Compton shoulder with a good signal-to-noise ratio for the first time, we try to constrain the torus parameters by spectral fitting only around the Fe–K line. The spectral model is the same as the input model; an absorbed power law and a smooth torus reflection or a clumpy torus reflection. The absorption and power-law parameters are fixed to the input value, except for a power-law normalization (the 6th parameter in Table 3). Metal abundance, turbulence velocity, and volume filling factor are also fixed to the input value. That is, free parameters are a power-law normalization, torus column density, torus inclination angle, and reflection normalization. We limited the energy band to 6.0–6.7 keV, and obtained the confidence contour.

Figure 17 shows a simulated SXS spectrum around the Fe–K line. The Compton shoulder is clearly resolved, and also $K\alpha_1$ and $K\alpha_2$ are separated, demonstrating the SXS power. Figure 18 shows confidence contours between column density and inclination angle for fitting with a smooth or clumpy torus. These figures demonstrate that spectral fitting only around Fe–K α line can constrain reflection parameters by using the Compton shoulder, and thus gives us a new tool to study the torus structure. Thus, together with the broad-band spectral fitting of the continuum, better constraint could be available. The behavior of contours are different between smooth and clumpy models. This is due to the different dependence on the column density for the Compton shoulder to core intensity ratio between two models as shown in Figure 6 right.

Therefore, this demonstrates that the correct modeling of the Compton shoulder is very important to probe the torus condition by using the Compton shoulder. In terms of this viewpoint, our model considers the different shape of a Compton shoulder between bound and free electrons and also that between atoms and molecules.

The MONACO framework on which our model is constructed has more advantages for exploring the torus model further. For example, X-ray reflection spectral modeling by ionized material and velocity structure of torus material can be implemented, as constructed for the simulation of AGN outflow (Hagino et al. 2015). Time history of reflection spectra after flares of the central engine can be also tracked, as applied for the Galactic center (Odaka et al. 2011). In contrast with a smooth torus model, a clumpy torus likely exhibits a fluctuation of the spectral shape for different azimuthal angles even with the same inclination angle. In a forthcoming paper, we will investigate to what extent such variations will appear. In this paper, we construct a simple torus geometry, but a more complex torus structure that has been recently suggested can be modeled. If the UV from the central accretion disk controls the innermost edge of a dusty tori, the shape of the inner part of the torus must be significantly different from that of the donut-like tori. Namely, a

strong anisotropy of the disk (Netzer 1987) makes the innermost edge of the torus concave (Kawaguchi & Mori 2010, 2011). At low latitudes of the torus (close to the midplane of the disk), the dusty torus exists very close to the outermost edge of the accretion disk. This region, where the rotational and turbulent velocities are likely large (some thousands km s^{-1} ; Kawaguchi 2013), may affect the line profile of emission lines (e.g., core to wing ratio), the time response of the line flux and profile, and the viewing angle dependence of the Fe–K lines. In a future paper, we will examine how the inner structure of the torus changes the overall results.

5. CONCLUSIONS

We construct an X-ray spectral model of a torus in an AGN with a Monte Carlo simulation framework MONACO. Two torus geometries of smooth and clumpy cases are considered. In order to reproduce a Compton shoulder accurately, MONACO includes not only free electron scattering but also bound electron scattering. Raman and Rayleigh scattering are also treated, and scattering cross sections dependent on chemical states of hydrogen and helium are included. Doppler broadening by turbulence velocity can be implemented. We compared our simulation spectra with a widely used X-ray spectral model MYTORUS, and found almost consistent results. We studied the dependence of reprocessed X-ray spectra, especially for the Fe–K line Compton shoulder on various torus parameters, such as hydrogen column density along a line on the equatorial plane, inclination angle from the line of sight, metal abundance, turbulence velocity for both smooth and clumpy cases, volume filling factor and clump scale radius for the clumpy case. The fraction and shape of the Compton shoulder depends on the column density, and the dependence is different between smooth and clumpy cases. Also, a weak dependence of the Compton shoulder shape on the inclination angle is seen. An equivalent width of the Fe–K core and the Compton shoulder and a fraction of the Compton shoulder largely depends on the metal abundance. Only a weak dependence of the Compton shoulder fraction is seen for the turbulence velocity, filling factor, and clump radius. We found that the Compton shoulder to line core intensity ratio mainly depends on the column density, inclination angle, and metal abundance. For instance, an increase of metal abundance makes the Compton shoulder relatively weak. Also, the shape of the Compton shoulder depends on the column density. Then, we present the ASTRO-H/SXS simulated spectra of Mrk 3 and found a clear Compton shoulder in the spectrum. Even with a narrow-band spectral fitting only around the Compton shoulder, we will be able to put some constraints on the torus geometry.

APPENDIX

A.1. Position Maps of Last Scattering of Compton Shoulder Photons

A.2. Comparison of Reprocessed Spectra Between Clumpy and Smooth Tori

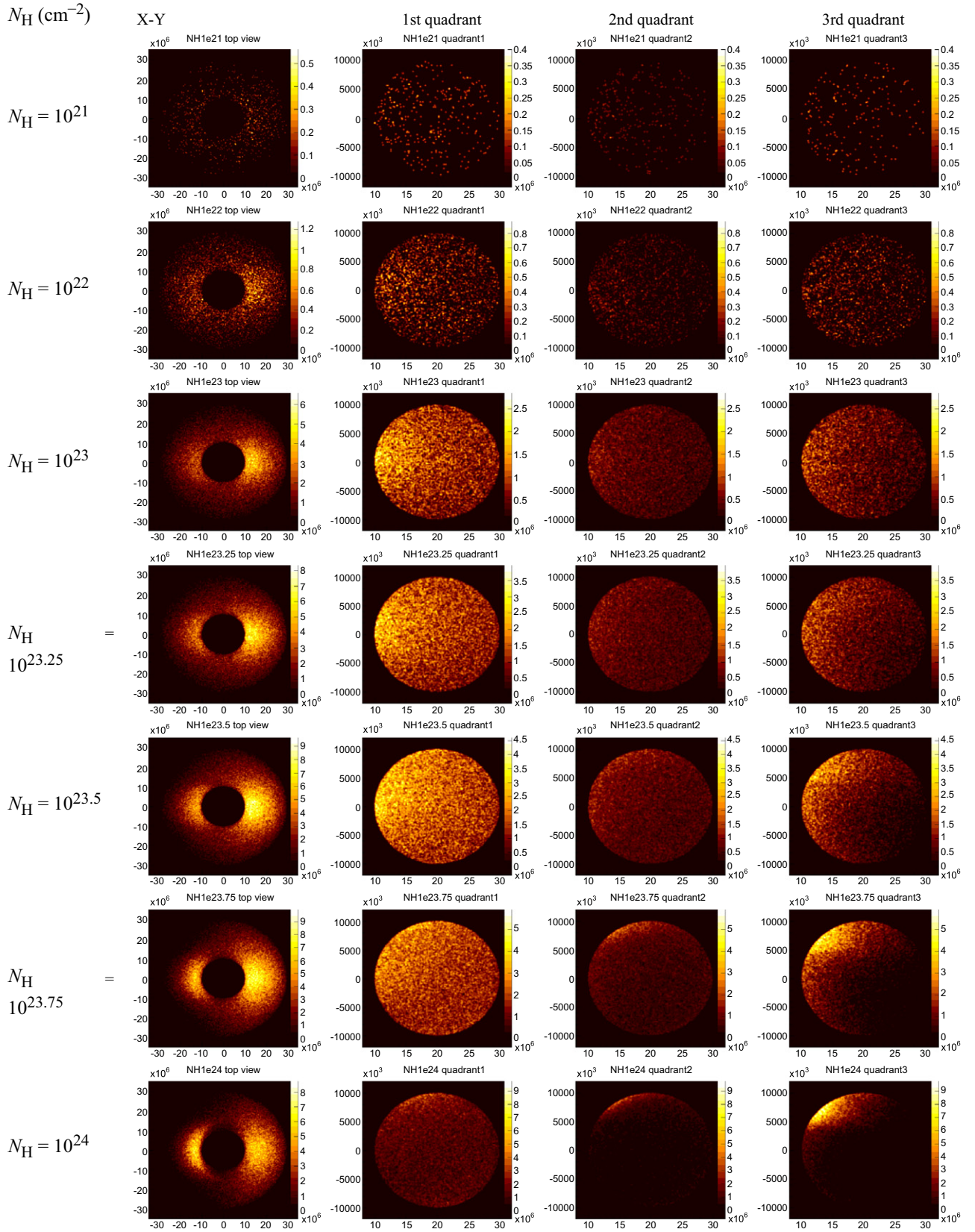


Figure 19. Position maps of last scattering of Compton shoulder photons in 6–6.39 keV for various column densities N_{H} . The observer is located toward the inclination angle of $\cos \theta_i = 0.1 - 0.2$ in the X-Z plane. The left panel is a map in the X-Y plane, where the observer is located toward the right direction. Middle left, middle right, and right panels are maps within the torus integrated over the first quadrant ($y > -x$ and $y < x$; i.e., close to the observer), second quadrant ($y > -x$ and $y > x$), and third quadrant ($y < -x$ and $y > x$; i.e., behind the central engine with respect to the observer), respectively.

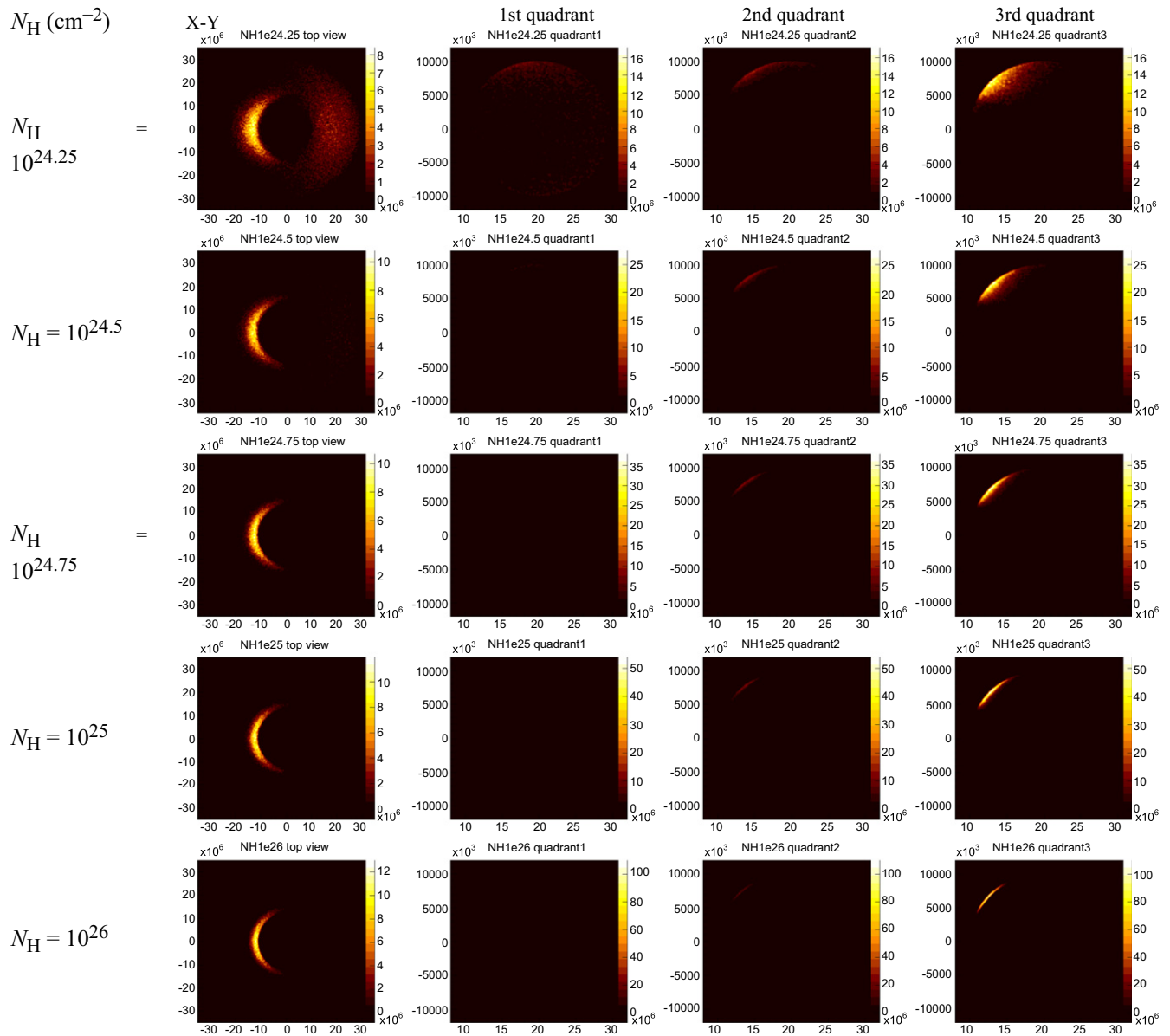


Figure 19. (Continued.)

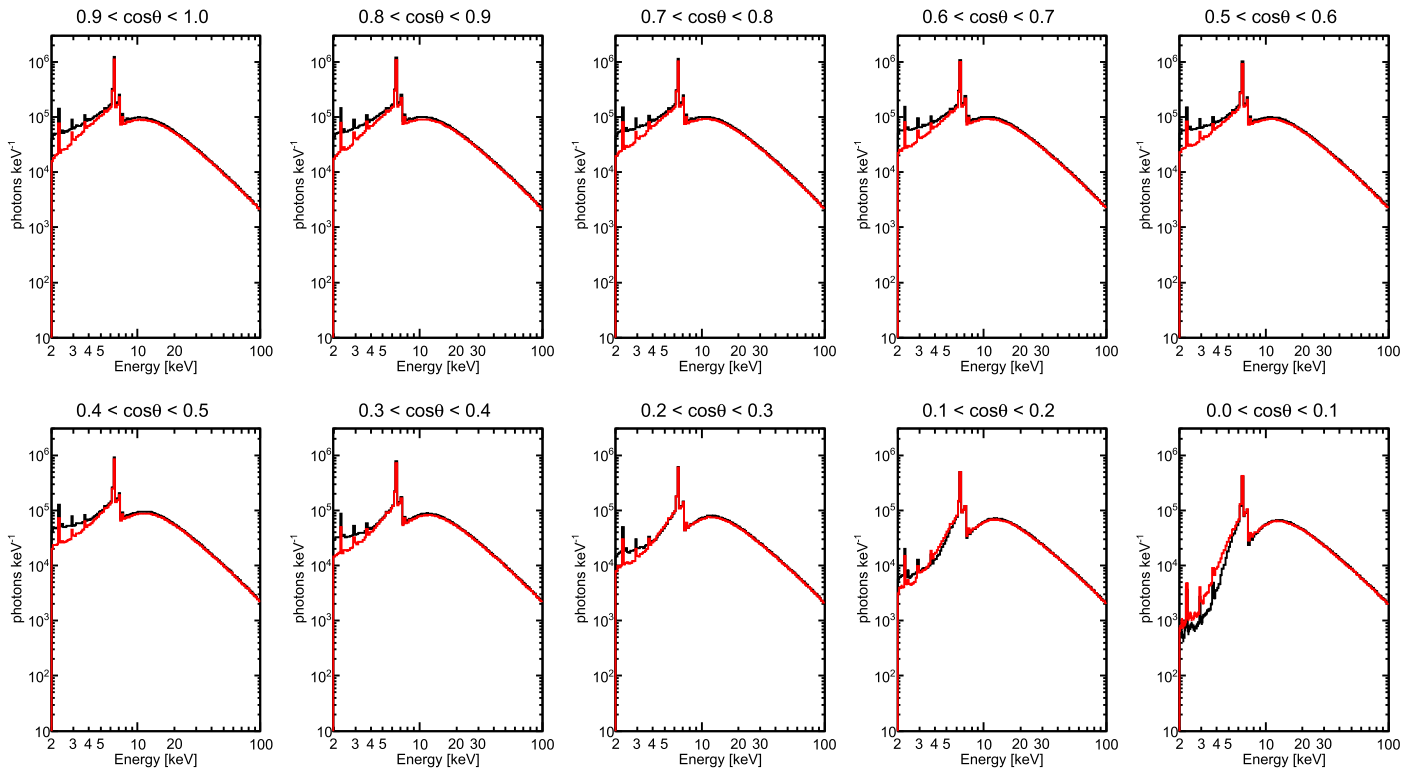


Figure 20. Comparison of reprocessed spectra between clumpy and smooth tori for various inclination angles of $\cos \theta_i = 0-1$ with a step of 0.1 in the case of $N_{\text{H}} = 10^{24} \text{ cm}^{-2}$. Black and red spectra correspond to smooth and clumpy tori, respectively.

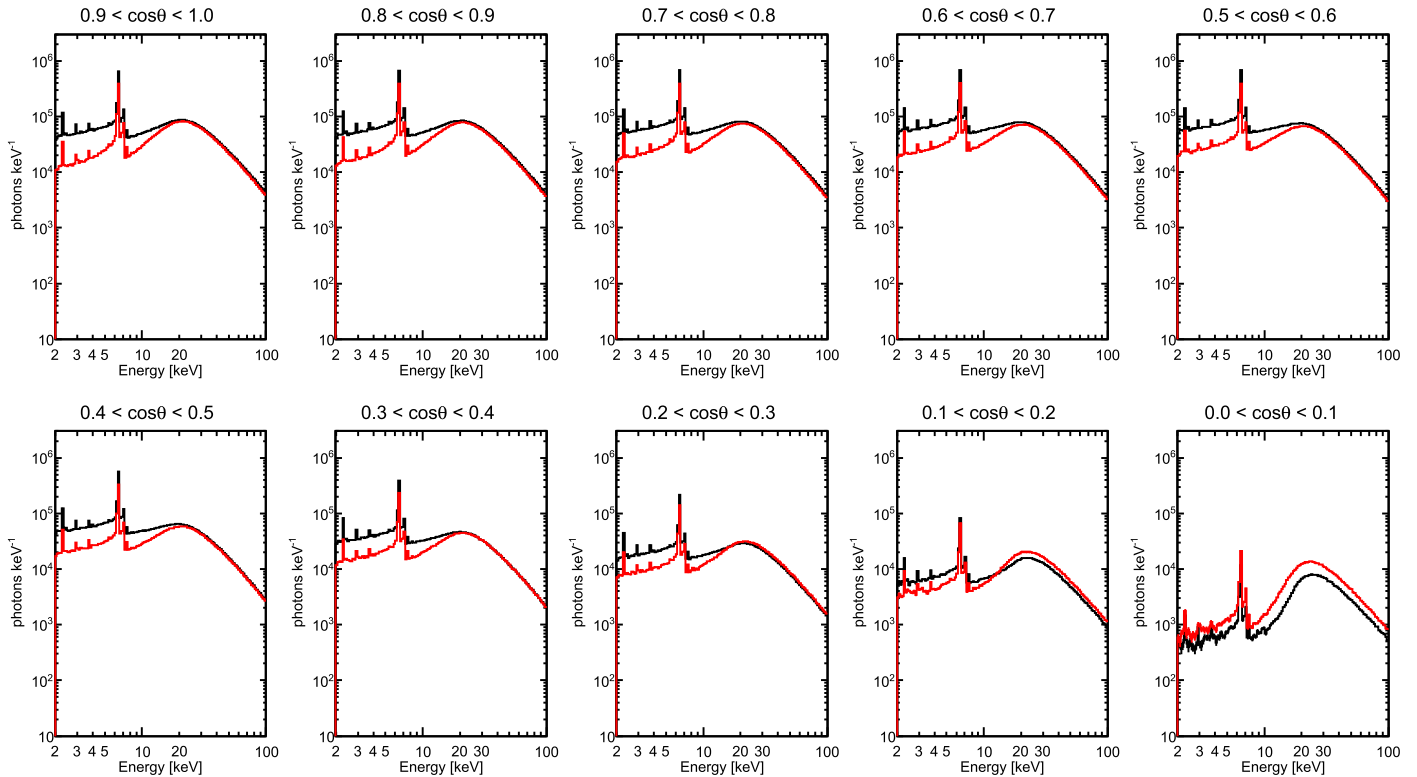


Figure 21. Same as Figure 20 but in the case of $N_{\text{H}} = 10^{25} \text{ cm}^{-2}$.

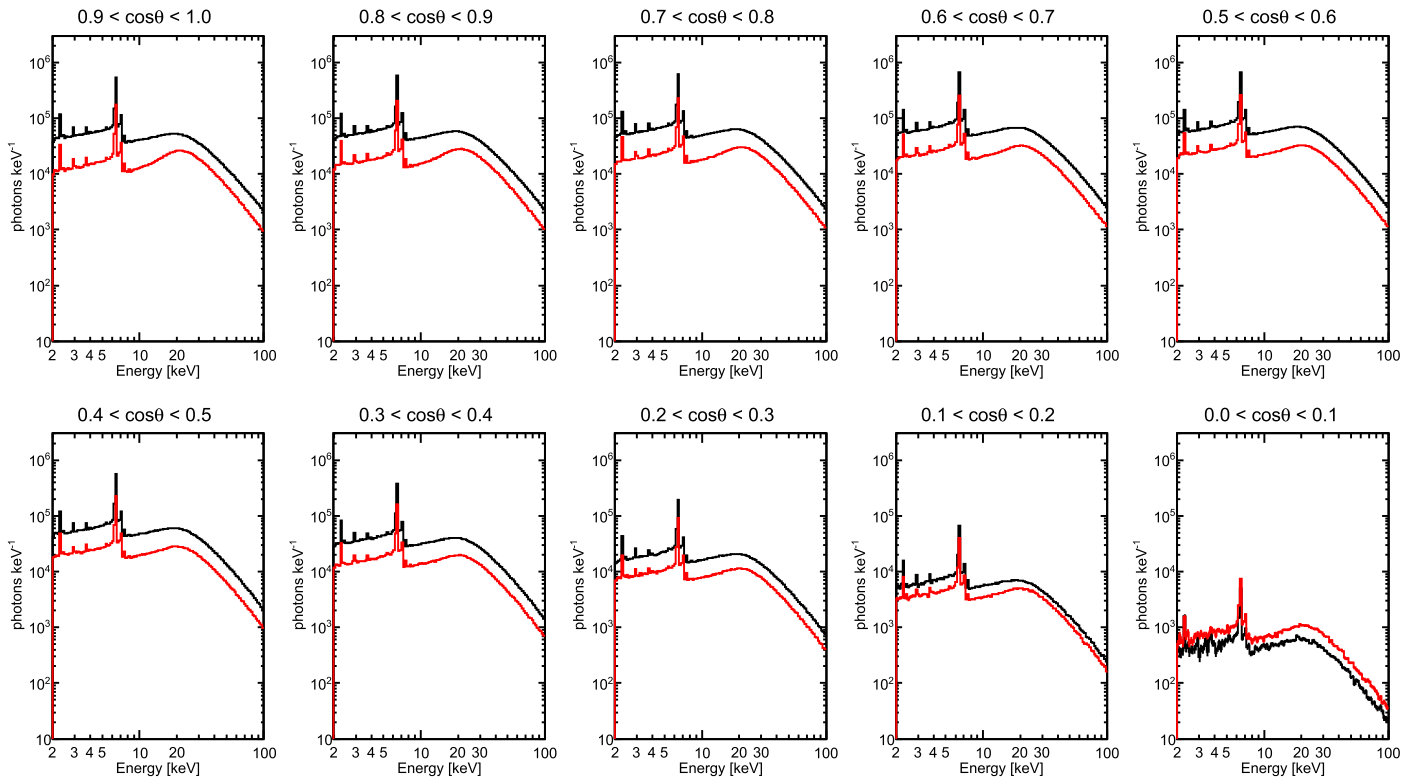


Figure 22. Same as Figure 20 but in the case of $N_{\text{H}} = 10^{26} \text{ cm}^{-2}$.

REFERENCES

- Agostinelli, S., Allison, J., Amako, K., et al. 2003, *NIMPA*, **506**, 250
- Allison, J., Amako, K., Apostolakis, J., et al. 2006, *IEEE Trans. Nucl. Sci.*, **53**, 270
- Anders, E., & Grevesse, N. 1989, *GeCoA*, **53**, 197
- Antonucci, R. R. J., & Miller, J. S. 1985, *ApJ*, **297**, 621
- Awaki, H., Anabuki, N., Fukazawa, Y., et al. 2008, *PASJ*, **60**, 293
- Awaki, H., Koyama, K., Inoue, H., & Halpern, J. P. 1991, *PASJ*, **43**, 195
- Barvainis, R. 1987, *ApJ*, **320**, 537
- Brightman, M., Baloković, M., Stern, D., et al. 2015, *ApJ*, **805**, 41
- Brightman, M., & Nandra, K. 2011, *MNRAS*, **413**, 1206
- Ertuğral, B., Apaydın, G., Çevik, U., Ertuğral, M., & Kobya, A. İ. 2007, *RaPC*, **76**, 15
- Fukazawa, Y., Hiragi, K., Mizuno, M., et al. 2011, *ApJ*, **727**, 19
- Hagino, K., Odaka, H., Done, C., et al. 2015, *MNRAS*, **446**, 663
- Hönig, S. F., Beckert, T., Ohnaka, K., & Weigelt, G. 2006, *A&A*, **452**, 459
- Ikedo, S., Awaki, H., & Terashima, Y. 2009, *ApJ*, **692**, 608
- Ivanenko, Y. N., & Geant4 Collaboration 2003, *NIMPA*, **502**, 666
- Kaspi, S., Brandt, W. N., George, I. M., et al. 2002, *ApJ*, **574**, 643
- Kawaguchi, T. 2013, arXiv:1306.0188
- Kawaguchi, T., & Mori, M. 2010, *ApJL*, **724**, L183
- Kawaguchi, T., & Mori, M. 2011, *ApJ*, **737**, 105
- Krause, M. O. 1979, *JPCRD*, **8**, 307
- Krolik, J. H., & Begelman, M. C. 1988, *ApJ*, **329**, 702
- Krolik, J. H., & Lepp, S. 1989, *ApJ*, **347**, 179
- Laor, A., & Draine, B. T. 1993, *ApJ*, **402**, 441
- Liu, Y., & Li, X. 2014, *ApJ*, **787**, 52
- Liu, Y., & Li, X. 2015, *MNRAS*, **448**, L53
- Magdziarz, P., & Zdziarski, A. A. 1995, *MNRAS*, **273**, 837
- Matt, G. 2002, *MNRAS*, **337**, 147
- Matt, G., Bianchi, S., D’Ammando, F., & Martocchia, A. 2004, *A&A*, **421**, 473
- Murphy, K. D., & Yaqoob, T. 2009, *MNRAS*, **397**, 1549
- Nandra, K., O’Neill, P. M., George, I. M., & Reeves, J. N. 2007, *MNRAS*, **382**, 194
- Nejkova, M., Sirocky, M. M., Nikutta, R., Ivezić, Z., & Elitzur, M. 2008, *ApJ*, **685**, 160
- Netzer, H. 1987, *MNRAS*, **225**, 55
- Odaka, H., Aharonian, F., Watanabe, S., et al. 2011, *ApJ*, **740**, 103
- Pier, E. A., & Voit, G. M. 1995, *ApJ*, **450**, 628
- Sunyaev, R. A., & Churazov, E. M. 1996, *AstL*, **22**, 648
- Sunyaev, R., & Churazov, E. 1998, *MNRAS*, **297**, 1279
- Takahashi, T., Mitsuda, K., Kelley, R., et al. 2014, *Proc. SPIE*, 9144, 914425
- Thompson, A. C., Attwood, D. T., Gullikson, E. M., et al. 2001, X-ray Data Booklet (Berkeley, CA: Lawrence Berkeley National Laboratory)
- Torrejón, J. M., Schulz, N. S., Nowak, M. A., & Kallman, T. R. 2010, *ApJ*, **715**, 947
- Watanabe, S., Sako, M., Ishida, M., et al. 2003, *ApJL*, **597**, L37
- Yaqoob, T., & Murphy, K. D. 2011, *MNRAS*, **412**, 277
- Yaqoob, T., Reeves, J. N., Markowitz, A., Serlemitsos, P. J., & Padmanabhan, U. 2005, *ApJ*, **627**, 156